

Article

Characterization of the Sedimentary Environment of the Shanxi Formation in the Southeastern Ordos Basin Revealed by Detrital Zircon and Geochemical Analyses

Jiandong Li ^{1,2}, Xianqing Li ^{1,2,*}, Wen Tian ^{3,*}, Chunhui Xiao ⁴, Yingfan Zhao ⁵, Jie Xiang ^{1,2} and Deyao Sun ⁵

¹ State Key Laboratory for Fine Exploration and Intelligent Development of Coal Resources, China University of Mining and Technology (Beijing), Beijing 100083, China; disheng369@126.com (J.L.)

² College of Geoscience and Surveying Engineering, China University of Mining and Technology (Beijing), Beijing 100083, China

³ Research Institute of Petroleum Exploration and Development, Shengli Oilfield Company, SINOPEC, Dongying 257015, China

⁴ Key Lab of Submarine Geosciences and Prospecting Techniques, MOE and College of Marine Geosciences, Ocean University of China, Qingdao 266100, China; xiaochunhui@ouc.edu.cn

⁵ College of Resource and Environmental Sciences, Hebei Normal University for Nationalities, Chengde 067000, China

* Correspondence: lixq@cumtb.edu.cn (X.L.); tianwenzi2008@163.com (W.T.);
Tel.: +86-010-62331854-8131 (X.L.); Fax: +86-010-62339208 (X.L.)

Abstract: The interpretation of the sedimentary paleogeographic environment of the Lower Permian Shanxi Formation (P₁s) coal strata in the southeastern Ordos Basin remains a subject of significant debate. In this paper, based on detrital zircon U–Pb source analysis, paleosalinity assessment, the sandstone modal composition, and other methods, we analyzed the P₁s source system and constructed a model of the sedimentary evolution. The findings reveal that the primary source of the clastic materials in the study area stems from a mixed-source within the recycling orogenic belt. During the deposition period, the Shanxi Formation developed two predominant material source systems: one in the north, primarily linked to the Paleo-Yinshan Fold Orogenic Belt (YFOB), and the other in the south, originating from the North Qinling Orogenic Belt (NQinOB). These two major source systems converged in the Yichuan–Fuxian area. From the early stages of the Shanxi Formation period (Shan1), there was a regional retreat of the sea in the area. The seawater receded in a southeastward direction, leading to a gradual reduction in the paleosalinity and Sr/Ba-ratio variability during the Shan1 period. The influence of the seawater diminished, transitioning into a deltaic depositional system. This shift towards a terrestrial lakeshore basin reached its full development during the Lower Xiashihezi period. This study concludes that the Shanxi Formation in this area represents the evolution of a deltaic depositional system originating from a shallow sea shelf. This evolution can be divided into three major stages: remnants of the shallow sea shelf, barrier island–lagoon–littoral, and deltaic deposition. Within this framework, the shoreline underwent frequent lateral migration, influencing a broad range of characteristics. In the vertical direction, numerous alternating sets of sandstone bodies and mudstone, shale, and coal beds formed, creating a significant relationship between coal hydrocarbon sources and reservoirs. This study also establishes the stratigraphic-sequence framework of the basin for this period. These results hold great importance for the expansion of natural gas exploration and development efforts.

Keywords: provenance analyses; detrital zircon; paleosalinity characteristics; paleogeography evolution; Ordos Basin



Citation: Li, J.; Li, X.; Tian, W.; Xiao, C.; Zhao, Y.; Xiang, J.; Sun, D. Characterization of the Sedimentary Environment of the Shanxi Formation in the Southeastern Ordos Basin Revealed by Detrital Zircon and Geochemical Analyses. *Minerals* **2023**, *13*, 1331. <https://doi.org/10.3390/min13101331>

Academic Editors: Marianna Kulkova and Dmitry Subetto

Received: 12 September 2023

Revised: 4 October 2023

Accepted: 10 October 2023

Published: 14 October 2023



Copyright: © 2023 by the authors. Licensee MDPI, Basel, Switzerland. This article is an open access article distributed under the terms and conditions of the Creative Commons Attribution (CC BY) license (<https://creativecommons.org/licenses/by/4.0/>).

1. Introduction

The Ordos Basin, situated in the southwestern region of the North China Craton (NCC), as illustrated in Figure 1, ranks as China's second-largest sedimentary basin, encompassing

an extensive area exceeding 25×10^4 km². This basin is characterized by relatively mild tectonic activity and is noteworthy for hosting ultra-low permeability lithological reservoirs, unconventional shale gas reservoirs, and tight oil and gas reservoirs. Since the 1990s, the northern section of the basin has yielded several substantial gas fields, boasting proven natural gas reserves exceeding 1000×10^8 m³, including Sulige, Yulin, Daniudi, Wushenqi, Shenmu, and Zizhou. These discoveries hold tremendous promise for further exploration and development.

In recent years, exploration efforts within the Ordos Basin have expanded towards its peripheral regions, resulting in significant breakthroughs in the southeastern sector of the basin [1]. Notably, the Yan'an gas field was discovered, alongside coal-bed methane and shale gas reserves, within the Daning–Jixian Block. Many scholars have undertaken research on and reevaluations of the geological conditions influencing the reservoir formation in this area [2–4]. Among these endeavors, a consensus has largely formed regarding the Carboniferous–Permian (Benxi–Taiyuan) terrestrial-to-marine sedimentary transition [5–7]. Nevertheless, controversies persist regarding the sedimentary environment and system patterns of the Permian Shanxi Formation, marked by the transition from sea to land. Four main viewpoints have emerged, suggesting a terrestrial lake delta depositional system [5,6], terrestrial river depositional system [7], offshore-lake-basin (shallow-land-shelf) delta depositional system [8,9], and marine-phase (land–sea transition phase) tidal flat–lagoon delta depositional system [10,11]. While these studies have provided valuable insights and knowledge, the investigation of the marine–land transitional-phase environment of the Shanxi Formation presents distinct challenges [12–14]. Tectonic movements led to a reconfiguration and consolidation of the depositional environments and phases during the Taiyuan Stage. Consequently, the Shanxi Formation is predominantly characterized by deltaic-phase deposition. A key question remains as to whether this delta's depositional backdrop was an offshore lake basin, an inland lake basin [15,16], or a shallow land shelf in the eastern part of the basin. The timing of the eastern part's marine regression, whether it rapidly transformed into an offshore lake or slowly regressed into a shallow land shelf, has implications [17,18]. Moreover, the study area is situated within the complex geological and tectonic context of a plate, featuring mixed source directions [19]. The uncertainties in geological understanding have constrained the exploration process for Upper Paleozoic coal gas in the southeast margin of the basin. Therefore, a comprehensive reassessment of the sedimentary and tectonic evolution of the southeast margin of the basin, particularly during the Permian Shanxi Formation's pivotal sea–land transformation phase, is imperative.

In the field of sedimentary evolution research, there have been notable advancements in recent years, particularly in the application of the U–Pb dating of detrital zircon, notably through LA-ICP-MS U–Pb dating. This analytical technique has played a pivotal role in advancing traceability analysis within sedimentary basins [20,21]. Moreover, it has been instrumental in investigating paleogeographic environments and basin evolution, and in ascertaining the rates of provenance-zone contributions [15,22,23]. In conjunction with U–Pb dating, various tools, such as Dickinson diagrams, paleocurrent directions, assessments of light- and heavy-mineral contents, the clastic composition, and geochemistry, have been deployed to decipher sedimentary basin histories. Some researchers have also explored sedimentary evolution by drawing upon stratigraphic and paleontological evidence, sedimentary structures, lithological attributes, and diagenesis, and by integrating various geochemical tests and analytical methods. These include calculating the paleosalinity using the boron elemental method, examining the Sr/Ba ratio, and investigating relationships between the boron, gallium, and rubidium contents [15]. However, the study of the marine–land transition phase within the Shanxi Formation presents distinctive challenges. Firstly, the basin's gentle topography, where sediment accumulates, often results in expansive shallow-water depositional areas. These regions are susceptible to widespread and frequent seawater disturbances, leading to the mingling of marine and terrestrial, thereby complicating differentiation efforts [15,24,25]. Secondly, the investigation of the

2. Geological Setting

The Ordos Basin constitutes a sub-tectonic unit within the North China Massif and is demarcated by distinct geological features [29–31]. It is bordered by the Kondalite Belt and the Yinshan Massif to the north, the Helanshan–Liupanshan Alluvial Belt to the west, the NQinOB to the south, and the Hengbei orogenic belt to the east, as shown in Figure 1b [33,34]. Based on the characteristics of the basement and prevailing tectonic morphology, the Ordos Basin can be subdivided into six sub-tectonic units: the Yimeng uplift, the Weibei uplift, the Jinxi flexure zone, the Yishang slope, the Tianhuan depression, and the western-margin alluvial zone (Figure 1) [35,36]. The stable Craton basement of the Ordos Basin was shaped around 5 billion years ago, with additional geological developments occurring approximately 1.85 billion years ago in the Early Paleoproterozoic period, evolving into a shallow-marine-platform phase. During the Late Paleozoic era, the Ordos Block transformed into an inland basin, influenced by the Qinling orogenic belt to the south. The Kongci rocks, situated in the northern part of the North China Block, are believed to have formed as a result of the collision between the Ordos Block and the Yingshan Block around 1.95 billion years ago [33,36]. In the south lies the NQinOB, which underwent significant magmatism during the Early Paleozoic period due to oceanic subduction, convergence, and the collision of arcs–continents. As the Late Paleozoic approached, the Qinling Block entered a comparatively tranquil period in terms of tectonic magmatism, with limited records of magmatic activity.

Our study area is situated on the southeastern edge of the Ordos Basin, forming a connection point between the Ordos Block to the north and the NQinOB to the south. This region represents a convergence area of several tectonic units and experienced a complex evolution of sedimentary tectonics during the Late Paleozoic. This evolution encompassed marine sedimentation, sea–land transitions, offshore lake basins, and inland depression lake basins, among others [31]. Notable sedimentary strata within the area include the Upper Carboniferous Benxi Formation, the Lower Permian Taiyuan and Shanxi Formations, the Middle Permian Shihezi Formation, and the Upper Permian Shiqianfeng Formation. The Shanxi Formation, in particular, features the Luotuobozi Sandstone at its top, which is interfaced with the Lower Shihezi Formation, and it exhibits a thickly bedded Camel’s Neck Sandstone deposit at its base (Figure 2).

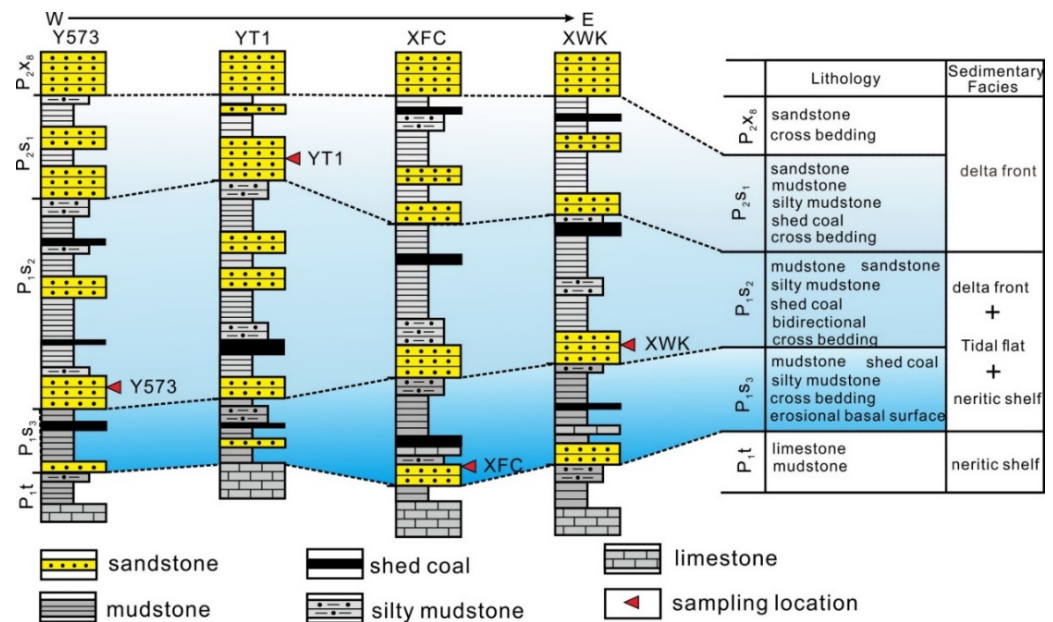


Figure 2. Stratigraphic column of the study area and selected samples (T753 and YT1 are exploration drilling sections in the study area, and XFC and XWK are exploration sections in the study area).

3. Sampling and Methods

Detailed field investigations were conducted, involving the collection of detrital zircon samples from two outcrops and two well cores. Specifically, samples were gathered from the Xiweikou (XWK) section in Hejin and the Xuefengchuang (XFC) section in Hancheng. Additionally, samples were obtained from the YT1 well and Y573 well within the Shanxi Formation, as depicted in Figure 2. In tandem with this, 53 core samples were meticulously collected for sandstone model analysis, while 32 core samples were procured for major-trace-element and clay-mineral testing, as shown in Figure 1c.

The zircon crystals were meticulously isolated through conventional heavy-liquid and magnetic techniques, followed by careful selection under a binocular microscope. Subsequently, target preparation and polishing were undertaken. The process for single-zircon-mineral separation utilized traditional heavy-liquid and magnetic methods [37]. The final step involved cathodoluminescence (CL) imaging and zircon LA-ICP-MS micro-area dating, conducted at the State Key Laboratory of Continental Dynamics, Northwest University, in Xi'an, China. The single-zircon LA-ICP-MS micro-area dating was carried out using an Agilent 7500 instrument. Zircon laser ablation followed a single-point-ablation sampling approach, employing the GeoLas 200M laser ablation system manufactured by MicroLas and ammonia as the carrier gas for the ablated material. The analysis method for zircon utilized 91,500 external-standard-calibration international standards [38,39], with the trace-element mass fraction Wist610 serving as an external standard. The laser spot beam had a diameter of 30 μm and operated at a frequency of 10 Hz, with a gas background acquisition time of 30 s for each sample point and a signal acquisition time of 40 s. Data processing was carried out using the Glitter (ver4.0) program (Macquarie University, Sydney, Australia), while the software Isoplot (ver3.0) (the American National Standard Substance Bureau) was employed to generate zircon age concordia diagrams and frequency distribution histograms. A total of 161 U–Pb age determinations were conducted.

For the major-element analysis, the sample was ground to a 200-mesh size in an agate mortar, dried at 110 °C for 3 h, and then placed in a sealed desiccator for cooling and stabilization. Subsequently, 0.7 g of powdered sample, 5.2 g of lithium tetraborate ($\text{Li}_2\text{B}_4\text{O}_7$) flux, 0.4 g of lithium fluoride (LiF) cosolvent, and 0.3 g of ammonium nitrate (NH_4NO_3) oxidizer were accurately weighed and mixed. The resulting mixture was placed into a platinum crucible, and 2–3 drops of lithium bromide (LiBr) release agent solution were added. The crucible was then covered and subjected to melting for 8 min using the ohyot-3KB automatic high-frequency fusion machine from Japan. After cooling, the samples were prepared for analysis. The major-element analysis was conducted at the State Key Laboratory of Continental Dynamics at Northwest University using the RIX2100 scanning automatic X-ray fluorescence spectrometer from Japan (RIGAKU). The fusion machine utilized was the Japanese OHYOT-3KB automatic high-frequency fusion machine. The analysis was controlled and monitored using BCR-2 and GBW07105 standard samples, ensuring an elemental-analysis accuracy better than 5%, and an instrument detection limit of 10^{-6} . Data replication was conducted for every ten samples [40].

The analysis of the trace elements Sr, Ba, B, and Ga, as well as of clay minerals, was performed by Xi'an Mineral Resources Supervision, Ministry of Land and Resources, using an XBS 4.0Kw X-ray fluorescence spectrometer and a PLASMA mass spectrometer for the ICP-MS.

For the identification of sandstone components, 30 thin sections were examined under a microscope. To ensure statistical accuracy, a minimum of 200 points were observed and counted in each sample, resulting in the collection of data from 23 sets of sandstone component identifications. Thin-section analysis was conducted at the State Key Laboratory of Continental Dynamics at Northwestern University, employing polarized light microscopy.

4. Results

4.1. Detrital Zircon U–Pb Ages

Zircon crystals originating from different sources exhibited variations in their Th and U contents, as well as in their Th/U ratios [41]. Specifically, metamorphic zircons typically exhibited Th/U ratios of less than 0.1, while magmatic zircons had Th/U ratios greater than 0.1. In the sampled zircons, the majority displayed Th/U ratios exceeding 0.1, accompanied by pronounced oscillation zones in their cathodoluminescence (CL) charts, indicating their magmatic origin. Only six zircon crystals exhibited Th/U ratios below 0.1, along with evident oscillation zones, suggesting the potential influence from later-stage metamorphic thermal events.

The zircon crystals in the XFC detrital samples displayed subrounded granular and subangular granular shapes (Figure 3a), indicating multiple transportation cycles and significant depositional abrasion. These zircon crystals ranged in size from 70 to 190 μm , with an aspect ratio falling within the range of 1–3. Their CL images typically exhibited uniform, weak banding or internal core–edge structures. The Th/U ratios of the zircons ranged from 0.09 to 2.45, with the vast majority (97.5% of the particles) displaying Th/U ratios greater than 0.1. The combined information from the CL imaging and Th/U ratios suggested that these zircons primarily originated from igneous protolith and metamorphic sources [41]. The zircon population was categorized into four major age groups: 447.3–304.9 Ma ($n = 21$), 2037.3–1780.9 Ma ($n = 24$), 2046.8–2009 Ma ($n = 8$), and 2531.7–2069 Ma ($n = 27$). The most prominent peak age observed was 391 Ma, followed by the ages 1995.2 and 2478.8 Ma (Figure 4a).

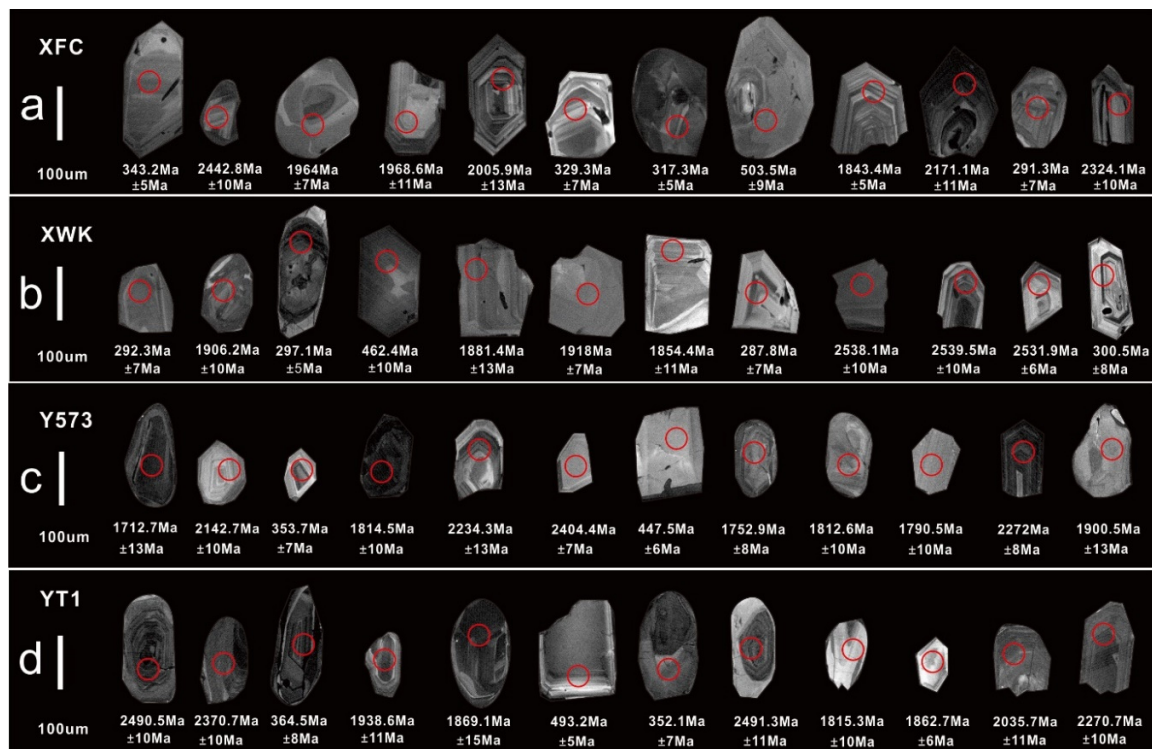


Figure 3. Representative CL images of the zircons: (a) sample XFC in the Shan3 Formation; (b) sample XWK in the Shan2 Formation; (c) sample Y573 in the Shan2 Formation; (d) sample YT1 in the Shan1 Formation. The circles represent the testing spots.

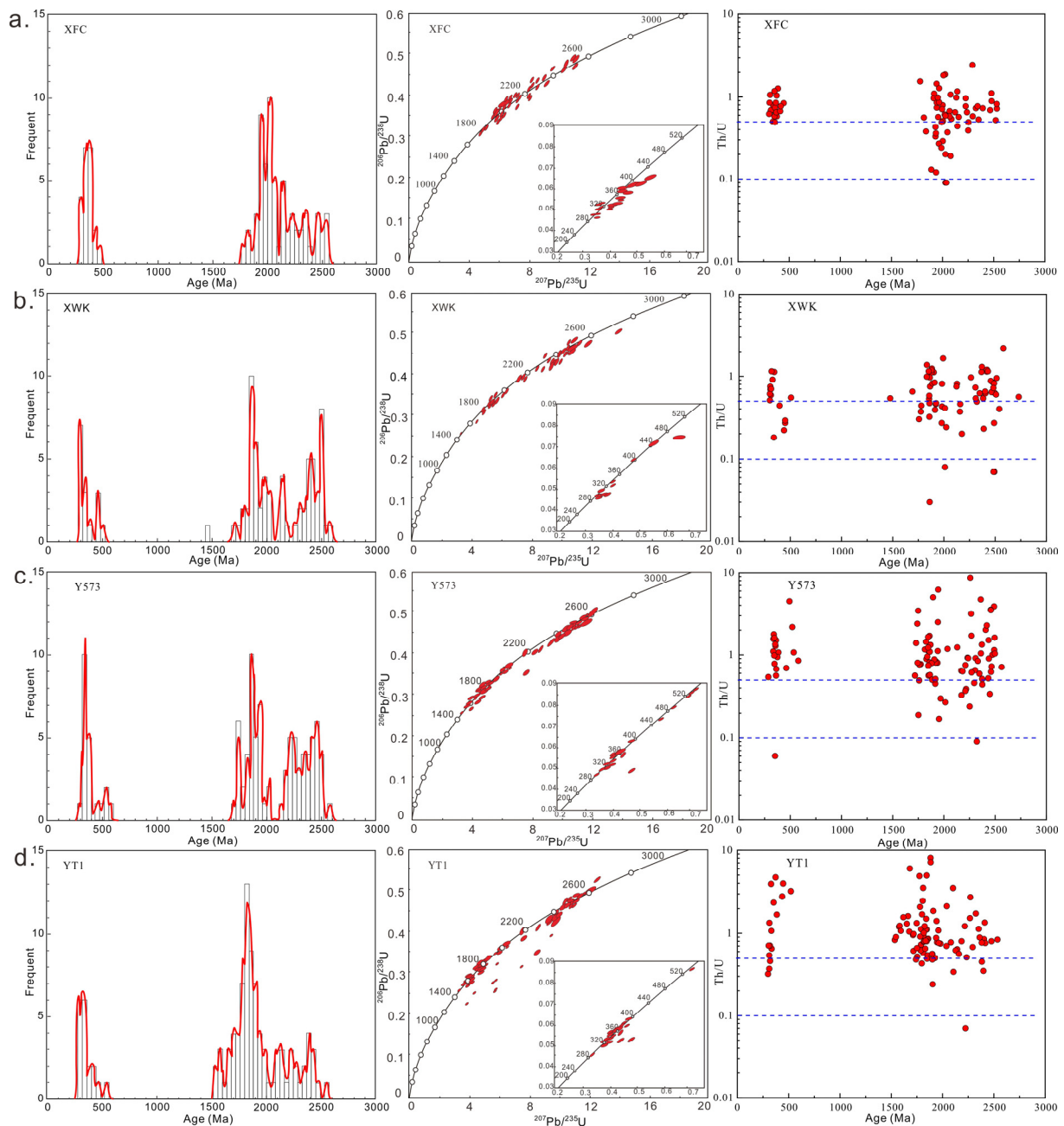


Figure 4. U–Pb concordia diagrams, U–Pb age patterns, and Th/U ratios for zircons separated from the following Shanxi Formation sandstones: (a) Shan3, XFC; (b) Shan2, XWK; (c) Shan2, Y573; (d) Shan1, YT1.

The detrital zircon crystals from the XWK section were predominantly subrounded or rounded in shape, indicative of short–medium-distance transport (Figure 3b). These zircons exhibited diameters ranging from 50 to 180 μm , with aspect ratios between 1 and 3. The majority of the zircons displayed uniform or oscillating characteristics in their cathodoluminescence (CL) images, and an overwhelming 95% of the particles possessed Th/U ratios greater than 0.1, suggesting their primary origin from igneous protoliths. The zircon age distributions revealed four prominent groups: 508.2–301.5 Ma ($n = 15$), 1993–1475.8 Ma ($n = 29$), 2264.2–2009.9 Ma ($n = 9$), and 2731–2308 Ma ($n = 28$). The most significant peak age observed was 1882.2 Ma, followed by the ages 2498.5 and 397 Ma (Figure 4b).

In the Y573 well, the majority of zircon crystals were subrounded, with some displaying subangular grains (Figure 3c). Their diameters ranged from 80 to 190 μm , with aspect ratios between 1 and 2.5. Most zircon crystals exhibited homogeneous or nebulous internal structures in the CL images, with a few displaying core–rim and sector structures. The Th/U values for the majority of crystals exceeded 0.4. Both the CL images and Th/U values indicated that the majority of zircon grains originated from magmatic sources [42]. The zircon ages (Figure 4c) spanned from 2564 Ma to 287 Ma, defining four primary age clusters: 2564–2310 Ma, 2295–2015 Ma, 1967–1718 Ma, and 579–287 Ma, with peak ages of 2490 Ma, 2257 Ma, 1894 Ma, and 385 Ma, respectively.

The zircon crystals from the YT1 well were predominantly subrounded, occasionally displaying rounded forms (Figure 3d), suggesting that they underwent short–medium–distance transportation. These zircon grains ranged in size from 80 μm to 180 μm . Most of them exhibited homogeneous or oscillatory characteristics, with zonings displaying Th/U ratios exceeding 0.1 (Figure 5), indicative of their magmatic origin. Out of 110 detrital zircon grains, 102 analyses displayed concordances greater than 90%. These ages ranged from 2535 Ma to 299 Ma, revealing four primary age groups: 2535–2037 Ma, 1978–1535 Ma, and 521–299 Ma, with notable age peaks at 2398 Ma, 1849 Ma, and 335 Ma, respectively (Figure 4d).

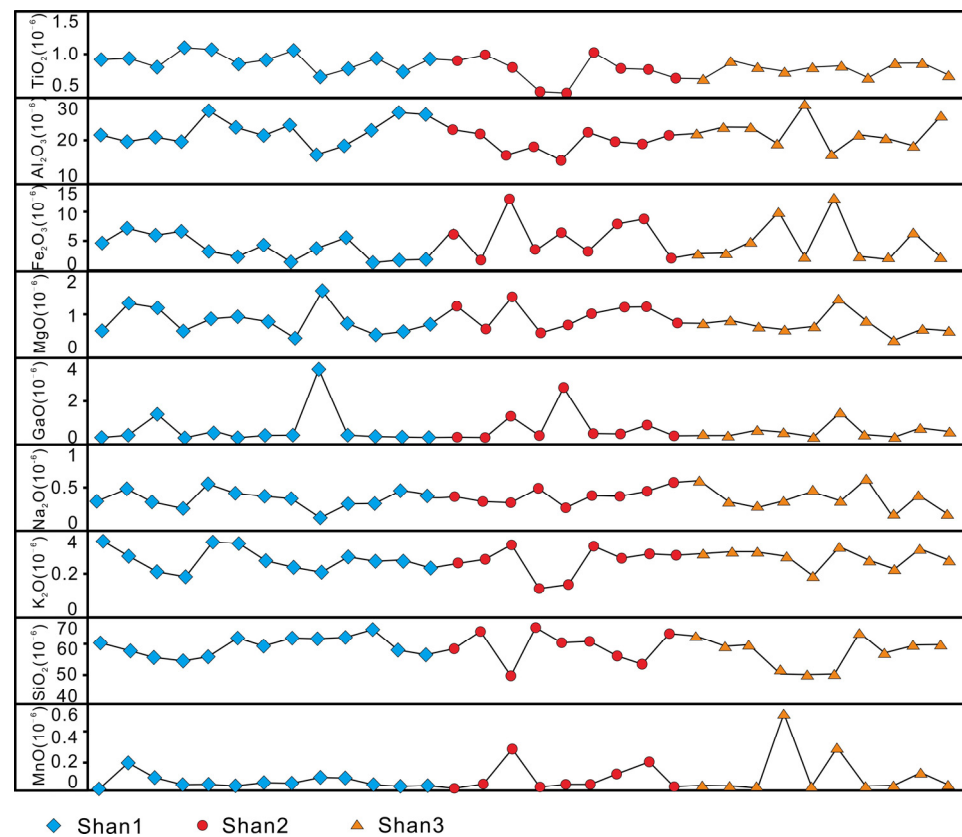


Figure 5. Distributions of major elements of Shanxi Formation.

4.2. The Major Elements of Sand–Mudstone

Figure 5 presents a comprehensive overview of 32 sets of major-element results. In general, feldspar, a primary constituent mineral of continental crust, is susceptible to alteration during deposition, leading to the depletion of elements such as K, Na, and Ca, while Al is retained in secondary clay minerals. In light of this, Nesbitt introduced the concept of the chemical index of alteration (CIA = $[\text{Al}_2\text{O}_3 / (\text{Al}_2\text{O}_3 + \text{CaO} + \text{Na}_2\text{O} + \text{K}_2\text{O})]$) as a means to quantify the degree of chemical differentiation. When CIA = 50, it suggests minimal chemical alteration, while a CIA = 100 indicates substantial chemical

differentiation, implying that alkali and alkaline elements have largely been leached out [43]. Cox introduced the index of compositional variation ($ICV = Fe_2O_3 + K_2O + Na_2O + CaO + MgO + MnO + TiO_2$) to characterize material composition traits and reflect the tectonic characteristics of the source region [43–45]. A high ICV value indicates that the rock components are less mature and rich in clay minerals, like montmorillonite and sericite, typically originating from regions with pronounced tectonic activity. Conversely, a low ICV value indicates a stable tectonic environment and a rock composition that lacks kaolinite clay minerals.

The sand–mudstone samples derived from the Shanxi Formation exhibited notably higher CIA values, ranging from 74.84% to 91.84%, with an average value of 85.31%. Simultaneously, the ICV values fell within the low–medium range, spanning from 0.21 to 1.18, with an average of 0.49. These observations collectively suggest that the sedimentary material primarily originated from relatively stable structural regions. Nevertheless, it is worth noting that some materials from areas characterized by strong tectonic activity were also incorporated. The majority of these rocks represent sedimentary products subject to significant weathering, while those containing weakly weathered particles offer a more accurate reflection of the source area characteristics. Furthermore, the majority of samples displayed low K_2O/Al_2O_3 ratios, ranging from 0.065 to 0.208, with an average value of 0.13. This observation suggests that the deposition process was relatively deficient in potassium-rich alkaline feldspar minerals, although a certain proportion of clay minerals were present. These findings align closely with the insights provided by the CIA and ICV indexes (Figure 6).

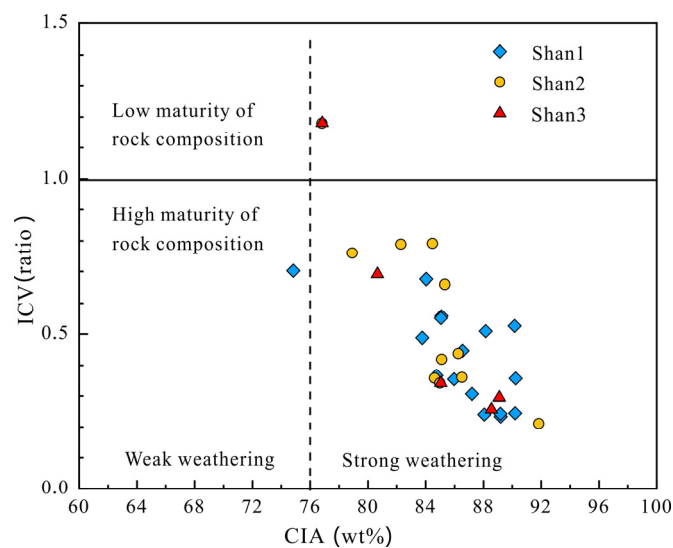


Figure 6. Diagram of CIA–ICV indexes of sand–mudstone in Shanxi Formation. CIA: chemical index of alteration; ICV: index of compositional variation.

4.3. The Characteristics of Paleosalinity

Calculating the paleosalinity based on the boron and clay mineral composition plays a pivotal role in identifying the sedimentary environment [46]. In this study, we employed Couch Equations (1) and (2) to compute the paleosalinity, which effectively mitigates the influence of non-clay minerals and accounts for variations in the adsorption capacities of different clay minerals. Additionally, the Sr/Ba ratio and B/Ga ratio were employed as sensitive indicators of the paleosalinity, serving as crucial tools for evaluating sedimentary environments:

$$S_p = 10^{(\log B - 0.11)/1.28} \quad (1)$$

$$B^* = B / (4X_i + 2X_m + X_k) \quad (2)$$

where S_p is the paleosalinity; B is the content of the B element; B^* is the correction value of the B element; X_i is the content of illite; X_m is the content of montmorillonite; X_k is the content of kaolinite.

The paleosalinity data reveal that the Shan1 sand–mudstone deposits predominantly originated from brackish–freshwater sedimentary environments, characterized by average Sr/Ba and B/Ga ratios and S_p values of 0.32, 1.26, and 8.87%, respectively. Similarly, the Shan2 sand–mudstone deposits were primarily associated with brackish–freshwater sedimentary conditions, exhibiting average Sr/Ba and B/Ga ratios and S_p values of 0.33, 2.41, and 10.63%, respectively. In comparison, the Shan3 sand–mudstone deposits were primarily indicative of brackish-water sedimentary environments, displaying an average Sr/Ba ratio, B/Ga ratio, and S_p value of 0.46, 2.94, and 21.91%, respectively.

4.4. Petrography and Modal Composition Analyses

In the lower section of the Shanxi Formation, one can observe dark-gray mudstone and carbonaceous mudstone, which are interbedded with gray, fine sandstone layers containing coal seams (Figure 7a). As we ascend to the upper part of the Shanxi Formation, gray-green and light-gray fine sandstone and mudstone become the predominant lithologies. These sandstones are characterized by high quartz contents, relatively poor sorting, and subangular grain shapes (Figure 7b). Generally, the mudstone exhibits a higher carbon content. In the XFC and XWK, one can observe lenticular gray-brown siltstone with scour surface structures and bidirectional cross-bedding features (Figure 7c–f).

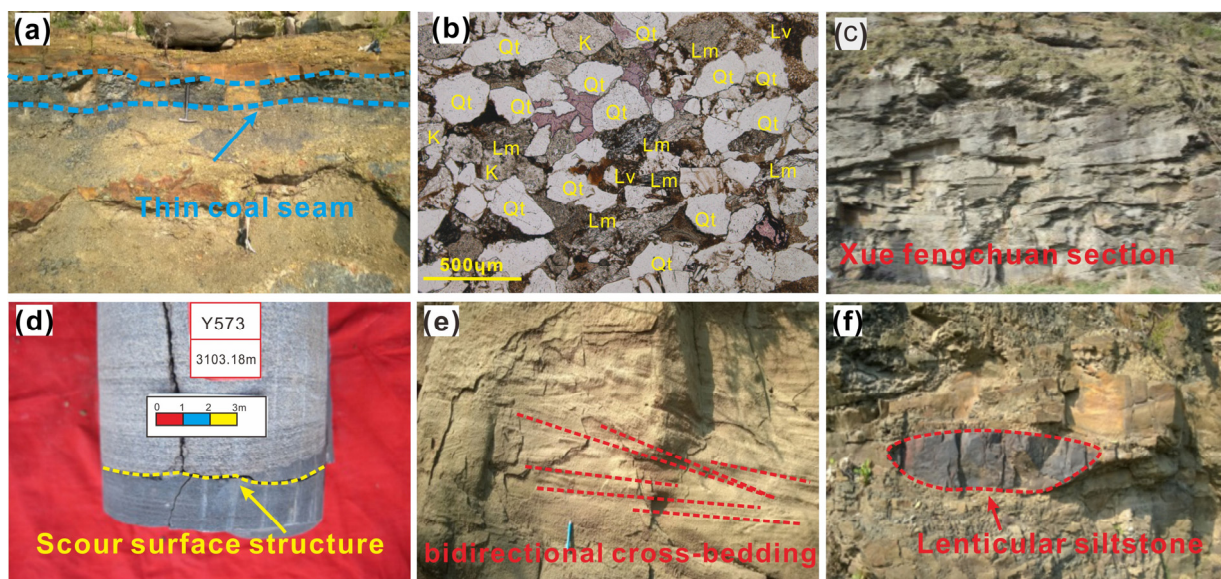


Figure 7. Petrographic images of the Lower Permian sandstones in the Xuefengchuang section of Hancheng and Xiweikou section of Hejin. K: K-feldspar; Qt: total quartz; Lv: volcanic rock fragments; Lm: metamorphic rock fragments. (a) Thin coal seam, Shan2, XWK; (b) Y573, Shan1, 2468.5 m, CTS; (c) channel-deposited thick sandstone, Shan1, XFC; (d) scour surface structure, Shan2, Y573; (e) pinnately intertwined, Shan3, XFC; (f) lenticular siltstone, Shan1, XWK.

4.4.1. Detrital Composition of Sandstones

Modal data were synthesized and presented using the Qt-F-L, Qm-F-Lt, Qp-Lv-Ls, and Qm-P-K ternary diagrams, with the impurity group contents in the samples remaining below 15% (Table 1). In the Qt-F-I diagram (Figure 8a) and Qm-F-Lt diagram (Figure 8b), the sandstone sample points were predominantly situated within the provenance region associated with recycled orogenic sources, with a few points falling within the stable continental provenance area and mixed-source zones. In the Qp-Lv-Ls diagram (Figure 8c), the majority of the sample points clustered within source areas linked to mixed orogenic

belts, volcanic-arc orogenic belts, collision suture zones, and fold–thrust-belt settings. Meanwhile, the Qm-P-K diagram (Figure 8d) indicated that all the sample points were positioned within the uplifted basement source area of the continental source region (Figure 8).

Table 1. Framework grain composition of the Shanxi Formation sandstones in the southeastern Ordos. Qt: total quartz; F: plagioclase feldspar and K-feldspar; P: plagioclase feldspar; K: K-feldspar; L: total lithic fragments excluding polycrystalline quartz; Qm: monocrystalline quartz; Lt: total lithic fragments; Qp: polycrystalline quartz (including chert); Lv: volcanic rock fragments; Ls: sedimentary rock fragments.

Sample	Formation	Qm	Qp	Qt	F	Lv	Ls	Lt	L
Y5	Shan1	65.76	2.41	68.17	6.85	7.47	17.51	27.39	24.98
Y6	Shan1	68.45	0.99	69.45	5.36	6.06	19.13	26.18	25.19
Y10	Shan1	82.16	1.75	83.92	1.17	2.34	12.57	16.67	14.91
Y12	Shan1	88.97	0.08	89.05	1.87	1.62	7.46	9.16	9.08
Y15	Shan1	73.72	0.73	74.45	2.55	8.03	14.96	23.72	22.99
YT1	Shan1	48.85	0.38	49.24	10.31	32.44	8.02	40.84	40.46
Y14	Shan1	59.60	0.33	59.93	0.00	24.17	15.89	40.40	40.07
Y186	Shan1	81.22	0.00	81.22	3.33	4.00	11.44	15.44	15.44
Y187	Shan1	67.00	1.00	68.00	0.00	0.00	32.00	33.00	32.00
Y188	Shan1	63.00	3.00	66.00	7.00	2.00	25.00	30.00	27.00
Y110	Shan1	83.43	2.30	85.73	2.88	1.96	9.44	13.69	11.39
Y188	Shan1	73.00	0.00	73.00	2.00	5.50	19.50	25.00	25.00
F4	Shan1	71.28	0.00	71.28	5.00	2.31	21.41	23.72	23.72
Y177	Shan1	77.81	1.83	79.63	2.87	6.27	11.23	19.32	17.49
Y187	Shan1	88.10	1.14	89.24	0.51	0.25	10.00	11.39	10.25
Y221	Shan1	79.40	0.00	79.40	2.00	7.40	11.20	18.60	18.60
Y256	Shan1	68.30	0.00	68.30	3.99	2.50	25.21	27.70	27.70
Y726	Shan1	64.79	0.00	64.79	4.23	8.45	22.54	30.99	30.99
Y632	Shan1	68.51	0.00	68.51	3.57	5.19	22.73	27.92	27.92
Y573	Shan1	76.41	0.00	76.41	2.66	5.98	14.95	20.93	20.93
Y563	Shan1	85.00	1.45	86.45	0.00	0.32	13.23	15.00	13.55
Y562	Shan1	86.55	0.00	86.55	1.79	4.48	7.17	11.66	11.66
Y554	Shan1	78.95	0.00	78.95	2.34	7.60	11.11	18.71	18.71
Y553	Shan1	70.88	0.93	71.81	3.99	0.80	23.40	25.13	24.20
Y351	Shan1	65.50	2.96	68.46	1.62	0.00	29.92	32.88	29.92
Y273	Shan1	71.94	1.38	73.32	2.57	1.78	22.33	25.49	24.11
Y263	Shan1	69.60	0.00	69.60	5.99	0.11	24.29	24.41	24.41
Y259	Shan1	67.00	0.00	67.00	2.00	6.00	25.00	31.00	31.00
Y257	Shan1	65.29	0.46	65.75	2.76	0.00	31.49	31.95	31.49
Y222	Shan1	61.54	0.00	61.54	3.85	5.13	29.49	34.62	34.62
Y636	Shan1	90.50	0.29	90.79	0.00	3.53	5.68	9.50	9.21
Y344	Shan1	55.97	1.22	57.19	2.79	1.66	38.36	41.24	40.02
Y276	Shan1	64.07	1.75	65.82	9.48	4.09	20.61	26.45	24.70
Y274	Shan1	48.27	0.00	48.27	2.67	17.60	31.47	49.07	49.07
FG2	Shan1	64.50	0.00	64.50	25.00	4.00	6.50	10.50	10.50
FG7	Shan1	48.64	0.00	48.64	5.36	14.00	32.00	46.00	46.00
FT1	Shan1	56.57	1.71	58.29	2.00	14.00	25.71	41.43	39.71
XF2	Shan1	55.56	0.00	55.56	0.00	3.00	41.44	44.44	44.44
Y110	Shan1	88.66	2.14	90.80	0.00	1.36	7.83	11.34	9.20
LT3-9-1	Shan1	53.75	4.38	58.13	33.75	0.00	8.13	12.50	8.13

Table 1. Cont.

Sample	Formation	Qm	Qp	Qt	F	Lv	Ls	Lt	L
LT3-9-2	Shan1	53.33	3.33	56.67	30.00	0.00	13.33	16.67	13.33
Y223-10	Shan1	53.68	5.79	59.47	26.32	1.58	12.63	20.00	14.21
FG5-2	Shan1	85.00	2.50	87.50	6.00	1.00	5.50	9.00	6.50
TT-6	Shan1	68.00	6.00	74.00	18.00	1.00	7.00	14.00	8.00
FG4-24	Shan1	65.00	5.00	70.00	21.00	0.00	9.00	14.00	9.00
FG5-53	Shan1	75.00	4.00	79.00	15.00	0.00	6.00	10.00	6.00
XFC-3	Shan1	53.00	2.00	55.00	38.00	0.00	7.00	9.00	7.00
Y5	Shan2	44.87	2.56	47.44	0.00	16.67	35.90	55.13	52.56
Y6	Shan2	69.57	0.62	70.19	2.48	8.07	19.25	27.95	27.33
YT1	Shan2	62.02	2.88	64.90	6.49	11.54	17.07	31.49	28.61
Y261	Shan2	37.57	0.00	37.57	0.00	0.00	62.43	62.43	62.43
Y112	Shan2	89.79	2.28	92.08	0.00	0.38	7.54	10.21	7.92
Y177	Shan2	88.10	2.12	90.21	0.00	0.26	9.52	11.90	9.79
Y731	Shan2	82.48	0.00	82.48	0.32	4.46	12.74	17.20	17.20
Y573	Shan2	78.68	0.00	78.68	2.20	6.59	12.53	19.12	19.12
Y552	Shan2	76.60	0.00	76.60	0.00	7.60	15.81	23.40	23.40
Y351	Shan2	53.19	4.26	57.45	4.26	0.00	38.30	42.55	38.30
Y259	Shan2	82.00	0.00	82.00	0.50	1.00	16.50	17.50	17.50
Y257	Shan2	60.04	3.11	63.15	2.28	0.21	34.37	37.68	34.58
Y222	Shan2	64.24	0.00	64.24	3.33	8.48	23.94	32.42	32.42
Y344	Shan2	47.64	1.29	48.93	5.15	0.86	45.06	47.21	45.92
FG7	Shan2	60.33	0.00	60.33	9.50	20.00	10.17	30.17	30.17
FT1	Shan2	56.00	1.33	57.33	0.00	18.33	24.33	44.00	42.67
XF2	Shan2	69.00	0.00	69.00	0.00	1.29	29.71	31.00	31.00
Y110	Shan2	84.01	3.28	87.29	1.77	2.00	8.94	14.22	10.94
Y104-3	Shan2	62.12	4.04	66.16	20.20	0.00	13.64	17.68	13.64
LT6-8-3	Shan2	48.00	4.00	52.00	38.00	0.00	10.00	14.00	10.00
XFC-2	Shan2	40.00	2.00	42.00	48.00	0.00	10.00	12.00	10.00
TT-8	Shan2	57.00	3.00	60.00	30.00	0.00	10.00	13.00	10.00
FG5-4	Shan2	83.00	2.50	85.50	9.00	0.00	5.50	8.00	5.50
FG5-54	Shan2	65.00	3.00	68.00	23.00	1.50	7.50	12.00	9.00
Y186	Shan3	87.04	0.09	87.13	1.86	1.36	9.64	11.10	11.01
Y110	Shan3	77.35	8.70	86.05	0.00	3.04	10.91	22.65	13.95
Y144	Shan3	94.99	0.00	94.99	0.00	0.00	5.01	5.01	5.01
Y196	Shan3	96.26	1.15	97.41	0.00	0.00	2.59	3.74	2.59
Y255	Shan3	84.67	0.00	84.67	1.34	0.00	13.99	13.99	13.99
Y634	Shan3	97.30	0.54	97.84	0.00	0.00	2.16	2.70	2.16
Y273	Shan3	61.84	5.26	67.11	1.32	2.63	28.95	36.84	31.58
FG2	Shan3	62.00	0.00	62.00	33.00	2.00	3.00	5.00	5.00
FT1	Shan3	71.00	1.00	72.00	0.00	5.00	23.00	29.00	28.00
Y110	Shan3	78.67	8.86	87.53	0.00	3.05	9.42	21.33	12.47
LT6-8-2	Shan3	50.00	3.00	53.00	36.00	1.00	10.00	14.00	11.00
LT8-9-1	Shan3	56.00	3.00	59.00	35.00	0.00	6.00	9.00	6.00
TT-7	Shan3	72.92	4.17	77.08	13.54	0.00	9.38	13.54	9.38
SYQ-1	Shan2	64.29	4.29	68.57	20.00	0.00	11.43	15.71	11.43

4.4.2. Characteristics of Light Minerals

Variations in the provenance of the basin resulted in differences in the light-mineral components of the sandstone within it. These differences can be employed to infer the provenance area and direction. The maturity of the composition and structure of detrital materials increases with longer transportation distances, making it a valuable tool for determining provenance.

The light-mineral content within the study area of Shan3 can be categorized into three regions (Figure 9a). To the south, in the Luochuan–Huanglong area, lithic sandstone and lithic quartz sandstone dominated, while, to the north, in the Yichuan–Fuxian region, lithic quartz sandstone and lithic sandstone were prevalent. In the central area, quartz

sandstone with a small amount of lithic quartz sandstone was the dominant lithology. The quartz content was relatively high, averaging 82.9%, while the feldspar content was less than 1%, and the clastic material comprised 12.81%. The central area exhibited the highest quartz content, reaching 92.2%. The light-mineral maturity index in the north of Yichuan–Fuxian County measured 7.7%, it measured 11.8% in the Xiaosizhuang region, and it measured 6.75% in the south of Luochuan–Huanglong. The light-mineral maturity index showed a gradient with the highest maturity in the central region, followed by lower values in the south and north, with the south being slightly less mature compared to the north. According to the flat distribution map of the light-mineral pie charts for Shan1 and Shan2 (Figure 9b,c), the extent of the lithic quartz sandstone and lithic sandstone increased gradually towards the north and south of the study area. In contrast, the region characterized by quartz sandstone and lithic quartz sandstone, which were more prevalent in the central area, diminished compared to Shan3, and was primarily distributed in the Fuxian–Xiaosizhuang Y224-well area.

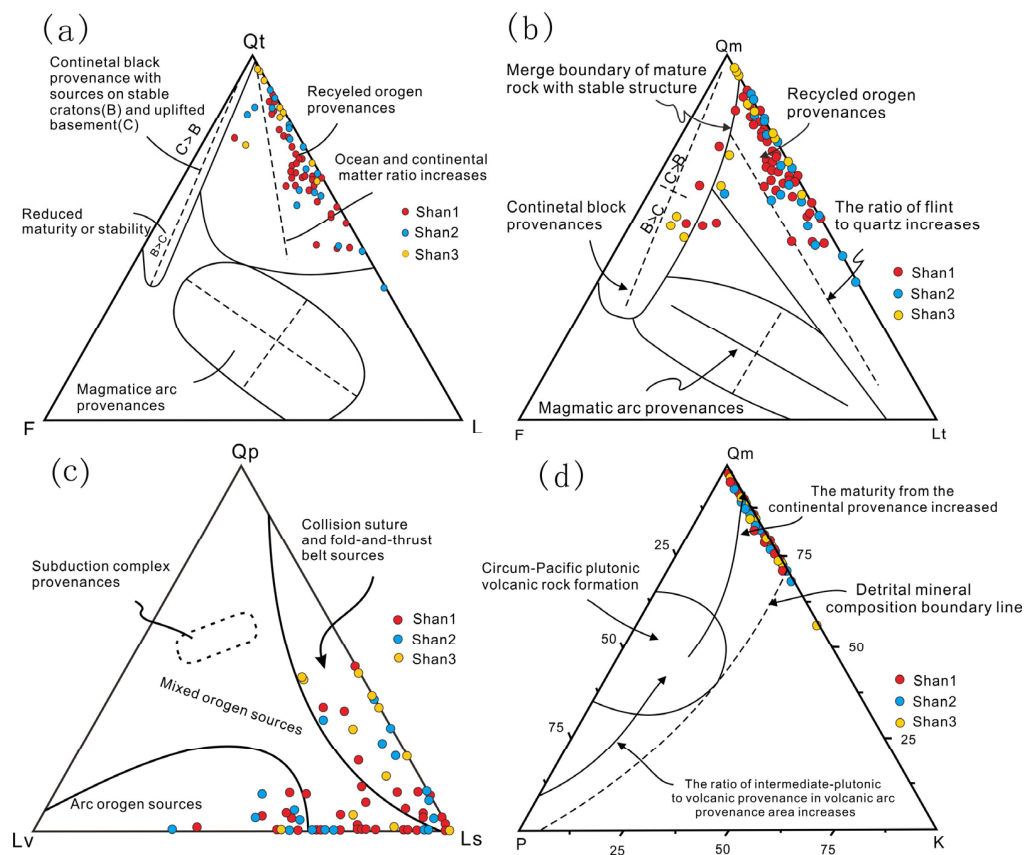


Figure 8. Ternary plots labeling the Shanxi Formation sandstone composition data. Qt: total quartz; F: plagioclase feldspar and K-feldspar; P: plagioclase feldspar; K: K-feldspar; L: total lithic fragments excluding polycrystalline quartz; Qm: monocrystalline quartz; Lt: total lithic fragments; Qp: polycrystalline quartz (including chert); Lv: volcanic rock fragments; Ls: sedimentary rock fragments. (a) QtFL Ternary diagram. (b) QmFLt Ternary diagram. (c) QpLvLs Ternary diagram. (d) QmPK Ternary diagram.

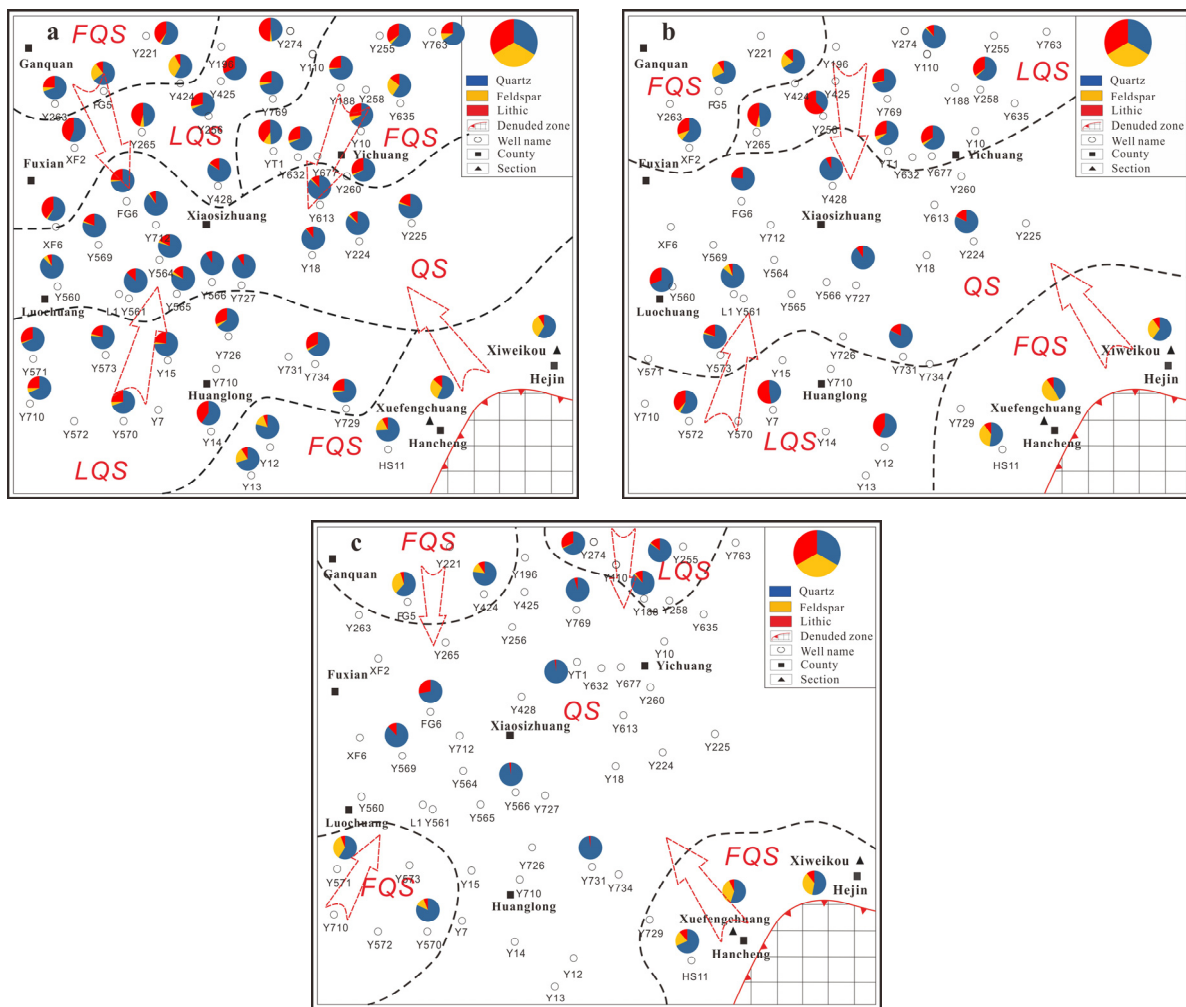


Figure 9. Pie chart of light-mineral distribution in Shanxi Formation. QS: quartz sandstone; FQS: feldspar quartz sandstone; LQS: lithic quartz sandstone. The black dotted line is the distribution range of different types of light minerals, and the red arrow is the source direction. (a) Distribution map of light minerals in Shan1. (b) Distribution map of light minerals in Shan2. (c) Distribution map of light minerals in Shan3.

5. Discussion

5.1. Sedimentary Provenance of the Shanxi Formation in the Southeastern Margin of Ordos

The modal composition of the Upper Paleozoic Shanxi Formation sandstone in the southeastern Ordos Basin indicates a predominantly mixed-orogenic source, comprising a significant proportion of recycled orogenic- and magmatic-arc contributions, along with a smaller fraction from continental sources (Figure 8). This finding aligns with the results of the multi-genetic debris components, reflecting the backdrop of a recirculation orogenic belt and its complex structure. This observation could correspond to the tectonic setting of the Yinshan region in the northern margin of the basin or possibly match the tectonic setting of the NQinOB. The geochemical characteristics of the rock revealed that most sediments experienced intense weathering, with some samples originating from less-weathered source areas (Figure 6).

The detrital zircon age distributions in all four samples exhibit strikingly similar age peaks and can be categorized into three major age groups: Palaeozoic (Late and Early Palaeozoic), Late Palaeoproterozoic (with a peak at around 1.8 Ga), and Neoproterozoic (peaking at approximately 2.5 Ga). Notably, there exists a significant gap in the ages from 1600 to 500 Ma within the two samples (Figure 10a). This gap may be associated with the age dis-

tribution of the Paleozoic sedimentary strata within the NCC [47–49]. Precambrian zircons might have undergone multiple recycling before being deposited in Phanerozoic sediments, whereas Phanerozoic zircons might have originated from the orogenic belts surrounding the NCC or nearby pre-Mesozoic recycled deposits. According to previous research findings, the Late Paleozoic period witnessed the deposition of continuous strata throughout the entire NCC, corroborating the reconstruction of the basin’s original configuration [50].

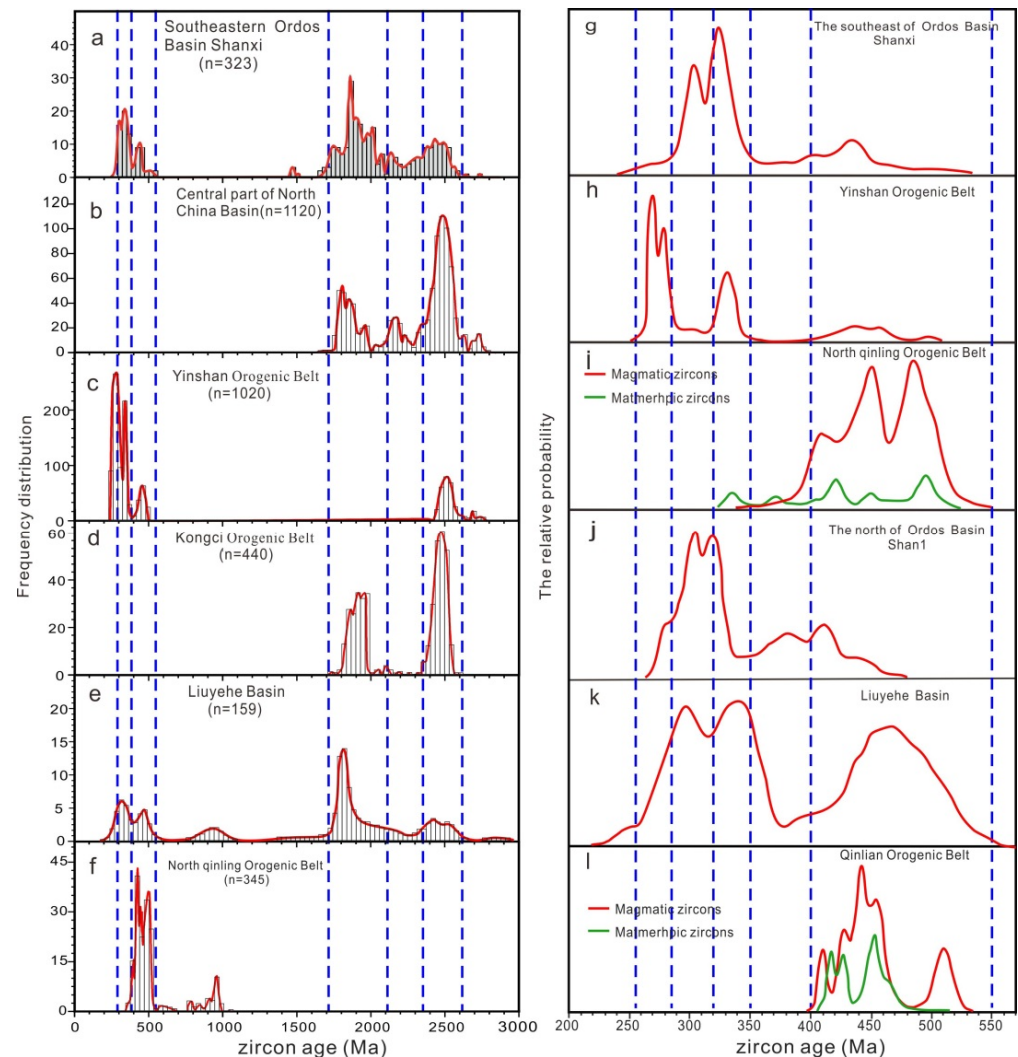


Figure 10. Contrasting relative-probability plots of zircon U–Pb ages. Date sources: (a,g) were from this experiment; (b) were from [40]; (c) were from [32]; (d,e) were from [40,51]; (f,l) were from [32]; (h,j) were from [30,52]; (i) were from [36]; (k) were from [49,53].

The Precambrian zircons from the Shanxi Formation constitute 77.1% of the total and are further subdivided into three age groups: 2700–2300 Ma, 2300–2100 Ma, and 2100–1600 Ma (Figure 10a). The majority of these zircons are magmatic, with only a few displaying characteristics of metamorphic zircons, as indicated by the CL images and Th/U values. When compared to the zircon ages from the orogenic belts surrounding the basin, it is reasonable to speculate that the 2700–2300 Ma and 2100–1700 Ma zircons in the study area may also have originated from the YFOB on the northern margin of the NCC [54,55] (Figure 10a–f).

Furthermore, the zircon age group from approximately 520–350 Ma exhibits a prominent peak at around 450–430 Ma and a less distinct peak around ~400–380 Ma (Figure 10g). This age distribution bears similarities to the zircon ages in the NQinOB but differs notably from the characteristics of the YFOB (Figure 10h). The NQinOB is characterized by extensive

metamorphic events at around 450 Ma and 430–400 Ma, with some ~407.5 Ma metamorphic zircons found in the NQinOB [48,56]. Based on these observations, it is plausible to suggest that the ~550–350 Ma detrital zircons from Shan1 may have originated from the NQinOB. The 520–350 Ma zircons likely formed during Paleozoic continental-collision and -accretion events in the NQinOB. Among them, the ~520–400 Ma zircons in the study area can be associated with the Ordovician–Early Devonian continental-collision and -accretion events in the NQinOB (Figure 10i), while the ~400–350 Ma zircons in the study area may be linked to Middle Devonian tectonic and thermal events in the NQinOB. It is worth noting that, although this zircon age group is found in the NQinOB (Figure 10l), scholars often favor the NQinOB as a source for the western Ordos Basin [42,57,58].

The presence of ~350–230 Ma magmatic events in the YFOB, caused by the collision orogeny between the Central Asian orogenic belt and the northern margin of the NCC, represents a distinct geological feature [16,21]. This magmatism is notably absent in other areas surrounding the Ordos Basin during the same period. Moreover, the widespread occurrence of the ~350–260 Ma zircon ages in the Shanxi Formation of the northern Ordos Basin (Figure 10j) suggests that these zircon ages likely originate primarily from the northern region of the basin [59]. However, notable differences exist in the detrital zircon age distribution of the ~350–260 Ma age group between the southeastern margin of the Ordos Basin and the YFOB (Figure 10h). Firstly, the intense magmatism in the YFOB during ~350–260 Ma was mainly concentrated around ~340–320 Ma and ~285–260 Ma, while the age distribution of detrital zircons in the southern Ordos Basin primarily falls within the ~320–285 Ma range (Figure 10g). Additionally, the proportion of ~320–285 Ma detrital zircons in the northern Ordos Basin is 7.1%, which is lower than that of the southeastern margin of the Ordos Basin (11%). Therefore, we suggest that the ~320–285 Ma detrital zircons in the southern and northern Ordos Basin have different source areas. The detrital zircons from the Shan1 members (~350–260 Ma) in the southern Ordos Basin may have originated from the NQinOB. Notably, a substantial number of ~350–260 Ma detrital zircons were found in Carboniferous–Triassic sandstones in the Liuyehe Basin (Figure 10k). Scholars such as Gao and Li have proposed that the Carboniferous–Triassic sandstone detrital zircons in the Liuyehe Basin have their source in the NQinOB and share the same origin as the southern Ordos Basin [48,53]. Secondly, although there are few reports of zircon age records of ~320–260 Ma in the NQinOB, the discovery of ~320–260 Ma zircons in the basin suggests that there may have been magmatic and metamorphic events in the NQinOB during this period that have yet to be fully revealed (Figure 10i) [42]. Additionally, Late Paleozoic zircons have been identified in the Liuyehe Basin, located in the strike-slip depression of the Shangdan Belt (Figure 10). Many scholars have hypothesized that the Liuyehe Basin received its sedimentary material from the NQinOB [53]. This further confirms that the NQinOB experienced tectonic and thermal activity during the Late Paleozoic. Furthermore, paleocurrent data from the Jushui River in Hancheng and Sanyuan Bridge in Chengcheng City indicate a predominant southeast–northwest flow direction, providing evidence that the NQinOB served as a source not only for the Liuyehe Basin in the south, but also for the Ordos Basin in the north [52,60]. Based on this cumulative evidence, it is reasonable to conclude that the detrital zircons from the ~290–350 Ma age group also have origins in the NQinOB, in addition to the YKOB and the central NCC. It is possible that the Late Paleozoic geological formations in the NQinOB were substantially eroded due to the strong denudation associated with late orogenic uplift.

5.2. Determination of Marginal Facies of Southern Provenance

Based on the CIA–ICV indexes, it is evident that the Upper Paleozoic Shanxi Formation sandstones and mudstones within the southeastern Ordos Basin primarily experienced strong weathering, with a minor proportion indicating weak weathering (Figure 6). This observation suggests that the mineral grains in these sediments were transported over significant distances, aligning with the compositional characteristics of light minerals. Weakly weathered feldspar grains are primarily distributed in the north and south of the

study area, while strongly weather-resistant quartz sandstone dominates in the central area (Figure 9). Bibbey-rock formations have been identified in the Upper Paleozoic strata of Zhouzhi, Liuyehe, and Jingyang counties in Shanxi Province [42,60]. Given the limited potential for long-distance transport, it is likely that these bibbey-rock formations originated from the NQinOB in the southern part of the Ordos Basin.

Lithofacies and logging facies analysis revealed that the principal sedimentary facies in the Permian Shanxi Formation are shallow-lake and delta-front facies. Shan3 is predominantly characterized by shallow lacustrine facies, while delta-front facies dominate in Shan2 and Shan1. Substantial variations in the connectivity of sandstones and sedimentary facies exist between different formations and the southern and northern areas (Figure 11). In the Y264-well area, the extent of the shallow lacustrine facies gradually decreases from Shan3 to Shan1, but there is an improvement in the connectivity of the sandstones. These differences may be attributed to varying provenances, with differing influence ranges of sources from the south and north. The enhanced supply of sediments from the southern source resulted in the extension of delta-front sandstone northward, eventually reaching the Y264-well area.

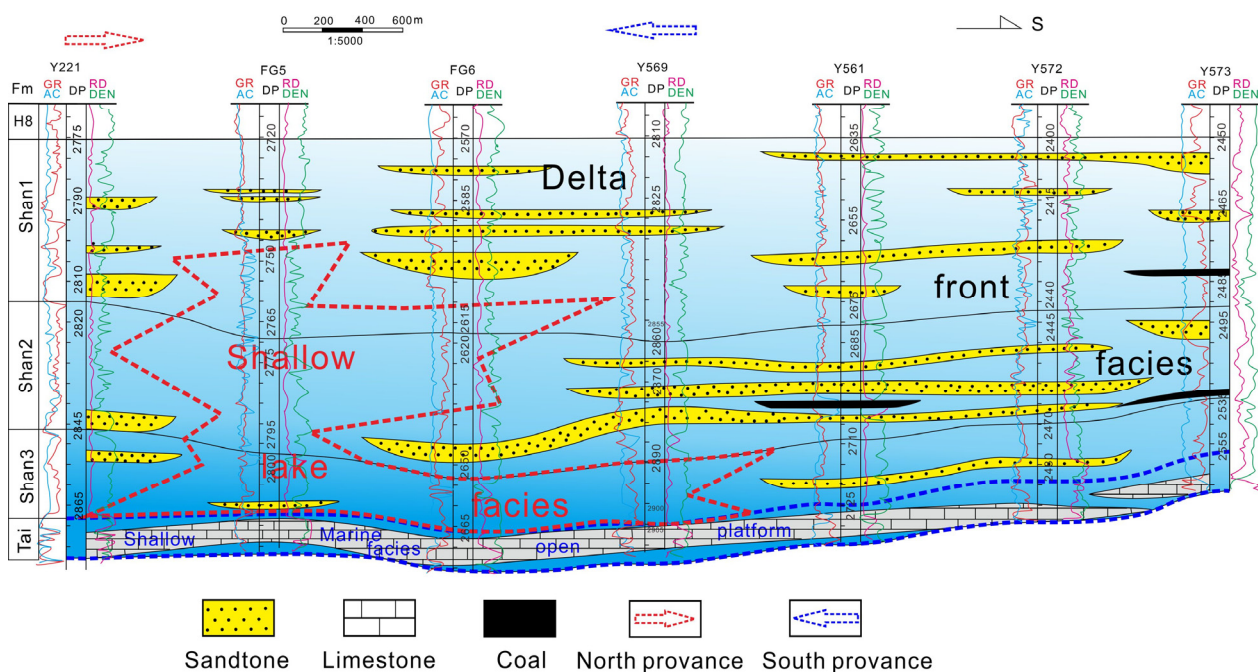


Figure 11. North–south-direction depositional facies section from Y221 to Y573 wells of Shanxi Formation. The red dotted line is shallow lake facies; the blue dotted line is shallow marine facies.

5.3. Tectono-Sedimentary Evolution during Early Permian Shanxi Formation

The formation of the Ordos Basin can be attributed to the subduction of oceanic plates beneath both the southern and northern margins of the NCC, resulting in the creation of two continental magmatic-arc belts: the NQinOB and the Inner Mongolia Paleo-uplift [24]. Provenance analyses of detrital zircon samples play a crucial role in unraveling the tectono-sedimentary evolution of the Ordos Basin [30,61–64].

Simultaneously, the NQinOB was believed to have experienced exhumation due to the continent subduction of the South Qinling Orogenic Belt and the NCC [30]. As previously discussed, Early Paleozoic detrital zircons supplied by the NQinOB were observed in the southeastern Ordos Basin, suggesting that the NQinOB was active until the Late Paleozoic, particularly during the Early Permian period (Figure 12a).

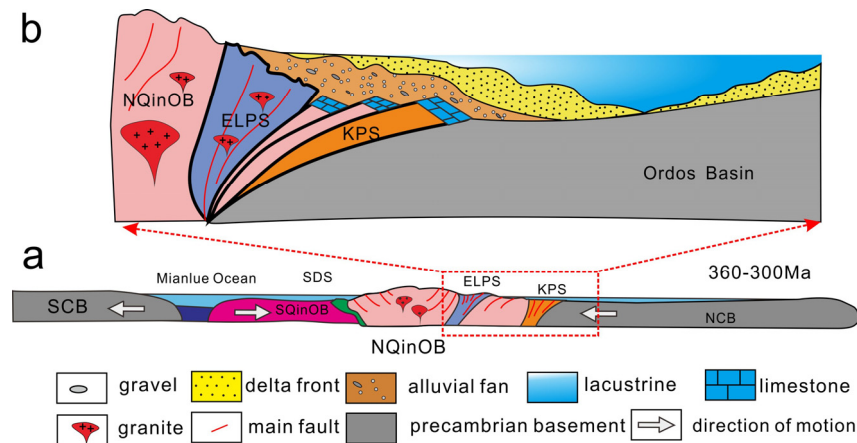


Figure 12. Tectono-sedimentary evolution in the NQinOB and southeastern Ordos Basin during the Paleozoic (modified after the literature [30,56]). ELPS: Erlangping suture; KPS: Kuangping suture; SDS: Shangdan suture; NQinOB: North of Qinling Orogenic Belt; SQinOB: South of Qinling Orogenic Belt; SCB: South China Block; NCB: North China Block. (a) Carboniferous tectonic profile of southern Ordos Basin. (b) Carboniferous tectonic profile in the study area.

This continent–arc–continent collision event resulted in the continuous uplift of the NQinOB and regional variations in the Early Permian depositional environment. In the southern Ordos Basin, subsidence and sedimentation were relatively pronounced. The paleogeography transitioned from a previous coastal marine basin system to a southeastward-deepening intracontinental lacustrine basin during the Early Permian Shanxi Formation (Figure 12b). Additionally, based on the spatial distribution patterns of the paleosalinity, it is evident that seawater receded from the southeast. The presence of syn-sedimentary detrital zircons in the XFC, XWK, YT1, and Y573 samples suggests intensive unroofing in the provenance region of the NQinOB and Inner Mongolia Paleo-uplift during the Early Permian. Approximately 100 m of strata was rapidly deposited in response to the rapid subsidence caused by rifting (Figure 12b). As the NQinOB continued to uplift and the provenance became more active, sedimentary facies in the southeastern Ordos Basin migrated northward, approaching the Fuxian–Yichuang area.

5.4. Stages of Sedimentary Tectonic Evolution and Geological Insights

The attribution of the sedimentary environment and the pattern of the sedimentary system in the Shanxi phase remain contentious. Building upon prior research and utilizing evidence from the stratigraphy, paleontology, sedimentary structure, geochemistry, and other characteristics, this study asserts that Shan3 represents a transitional phase within a land–sea interface, while Shan2 and Shan1 denote a deltaic depositional system within terrestrial lakes and basins. This classification is supported by several key observations.

Field investigations in Shanxi Province, near the eastern basin edge, revealed three distinct marine intercalations in the Shanxi Formation. These intercalations primarily consist of siliciclastic rocks, limestones, calcareous mudstones, and fossiliferous mudstones displaying marine facies. Notably, the marine facies diminish gradually from south to north and are absent north of Taiyuan [10]. The Ordos Basin, a component of the North China Massif, shared a similar aquatic environment with the Luliang area in the eastern sector of the Shanxi Group [65]. There were no significant barriers hindering the flow. However, as deposition in the Shanxi Group neared completion, the uplifts of Luliang and Weibei successively occurred, creating drainage systems in the southeast. Consequently, seawater regressed in a southeastward direction.

In the Shan3 Formation of the Daniudi gas field in the northeastern part of the Ordos Basin, powder crystal dolomite and mud crystal iron dolomite are prevalent. Notably, sea lilies and foraminiferal bone fragments were discovered in the mudstones of the Shan2 Formation in the D12 and D3 wells [66]. Additionally, echinoderm and brachiopod fossils

were found in the mudstones of the Shan2 Formation in the Y48 well and S212 well [10,67]. Furthermore, sunnipedes and silicicolous radiolarians were identified in the mudstones of the Y31 well in the eastern part of the Ordos Basin [31]. These paleontological findings, commonly associated with marine strata, have been reported in the literature within the Ordos Basin. Although their distribution is limited and they might have been transported by tidal currents, they do suggest that the Shan2 Formation at the eastern margin of the Ordos Basin was influenced by sea transgression.

Field observations of the Shanxi Formation section in the southeastern part of the basin, specifically in XFC, reveal a distinct pinnately interbedded stratigraphy (Figure 7e). Additionally, numerous primary sedimentary structures related to the marine sedimentary environment, including tidal laminations and pinnately interbedded laminations, were observed in the Shanxi Formation sections around Sanyeonqiao, Gancaoshan, and XWK. These findings indicate the presence of sea intrusion during the early period of the Shanxi Formation in the southeastern part of the basin.

Paleosalinity discrimination can be achieved using markers such as the Sr/Ba and B/Ga ratios and S_p values. Different scholars apply varying criteria for classifying the water body salinity. In this paper, considering previous research, Sr/Ba = 0.5, B/Ga = 33, and $S_p = 33\%$ were used as the threshold between freshwater and mixed water [10,32,68,69]. Based on the paleosalinity distribution diagram of the Shanxi Formation, it was observed that Shan1 and Shan2 exhibited brackish–freshwater sedimentation, while Shan3 displayed brackish-water sedimentation. Moreover, the trend of the paleosalinity variation differed slightly in each sub-layer of the Shanxi Formation, with a gradual decrease in the paleosalinity from Shan3 to Shan1 (Figure 13). Three distinct transgression–regression cycles were evident in the Shanxi Formation, with the transgression scale of Shan1 being smaller than those of Shan2 and Shan3. Additionally, the maximum flooding surface appeared during the middle–late stages of each cycle (Figure 13). A comparative analysis of the paleosalinity across different strata and areas within the Shanxi Formation revealed a gradual decrease from south to north and from west to east within the Ordos Basin. This difference was more pronounced between Shan3 and Shan2 than in Shan1, and it nearly disappeared in the Shan1 Formation. When comparing the Shanxi Formation from bottom to top (Figure 14), a similar but not identical trend in variation was observed. These characteristics suggest the development of intermittent transgressions in the Shanxi Formation, accompanied by sea–lake replacement events. The presence of extensive fluvial–deltaic facies in the Ordos Basin, influenced by the Inner Mongolia Paleo-uplift in the northern part of the basin and the NQinOB uplift in the southern part, led to the development of continental runoff and the gradual formation of inland lake basins. Only the southeastern edge of the study area was affected by transgression and regression.

In contrast to the Shanxi Formation, the Shihezi strata exhibited a typical freshwater sedimentary environment, while the Taiyuan–Majiagou strata represented a typical saline-water sedimentary environment (Figure 14) [70]. Examining the vertical evolution sequence, which progresses from the Majiagou Formation to the Taiyuan, Shanxi, and finally Shihezi Formations, it becomes evident that the sedimentary environment gradually transitioned from marine facies to transitional facies, ultimately evolving into continental facies (Figure 14) [31,32,70]. While traces of seawater were still present in the Shanxi Formation, the seawater had completely retreated from the basin by the base of the Shihezi Formation, marking the basin's transition into the continental-lake-basin stage.

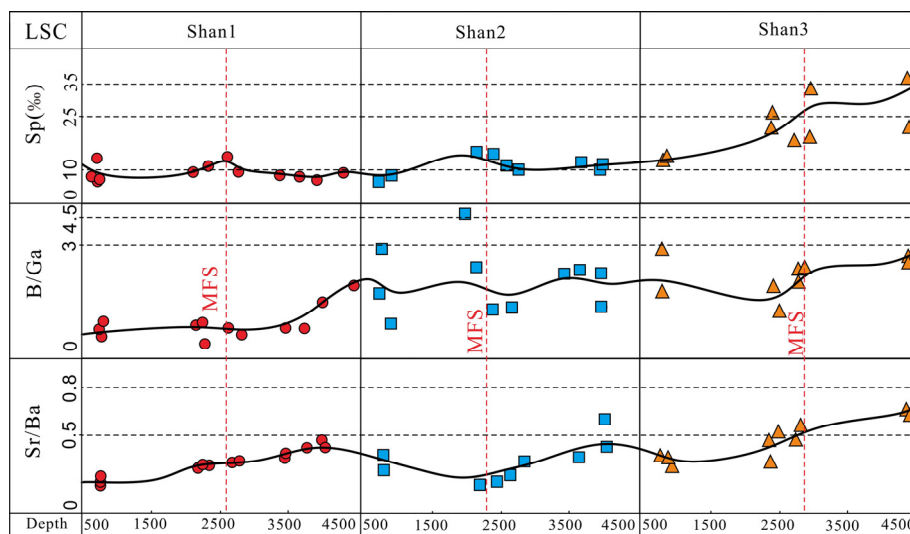


Figure 13. Sr/Ba and B/Ga ratios and S_p values of Late Paleozoic Shanxi Formation in eastern Ordos Basin. MFS: maximum flood surface.

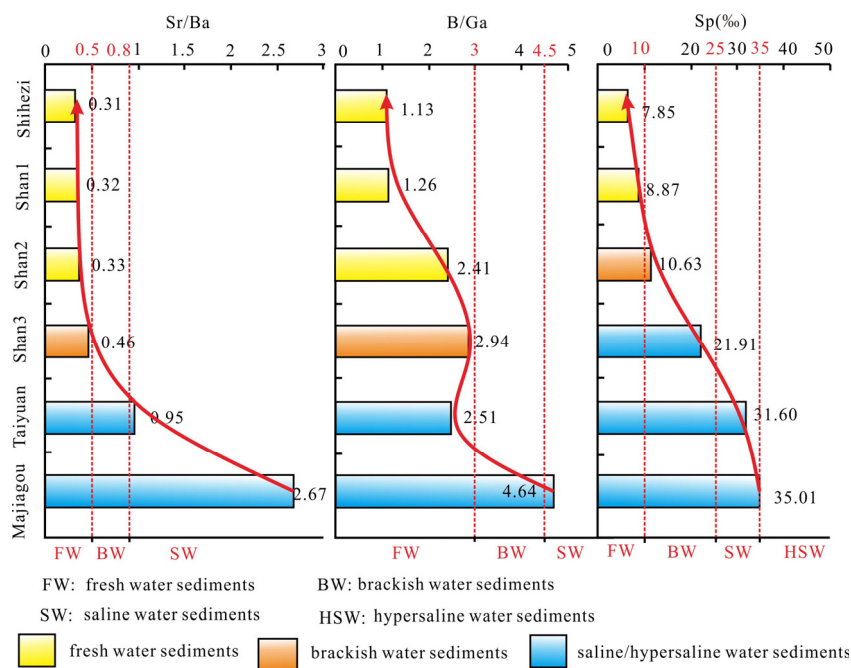


Figure 14. Sr/Ba and B/Ga ratios and S_p average values of Late Paleozoic Formation in eastern Ordos Basin (the Sr/Ba dates of Shihezi, Taiyuan, and Majiagou are cited from the literature [31,32,65]).

5.5. Paleogeography Evolution and Geological Insights

Considering the regional tectonic and sedimentary characteristics of the Late Paleozoic in the Ordos Basin, the sedimentary–tectonic evolution of the Shanxi Formation in this area was divided into three distinct stages (Figure 15) [70]. Furthermore, a tectonic–sedimentary evolutionary sequence for the Shanxi Formation was established.

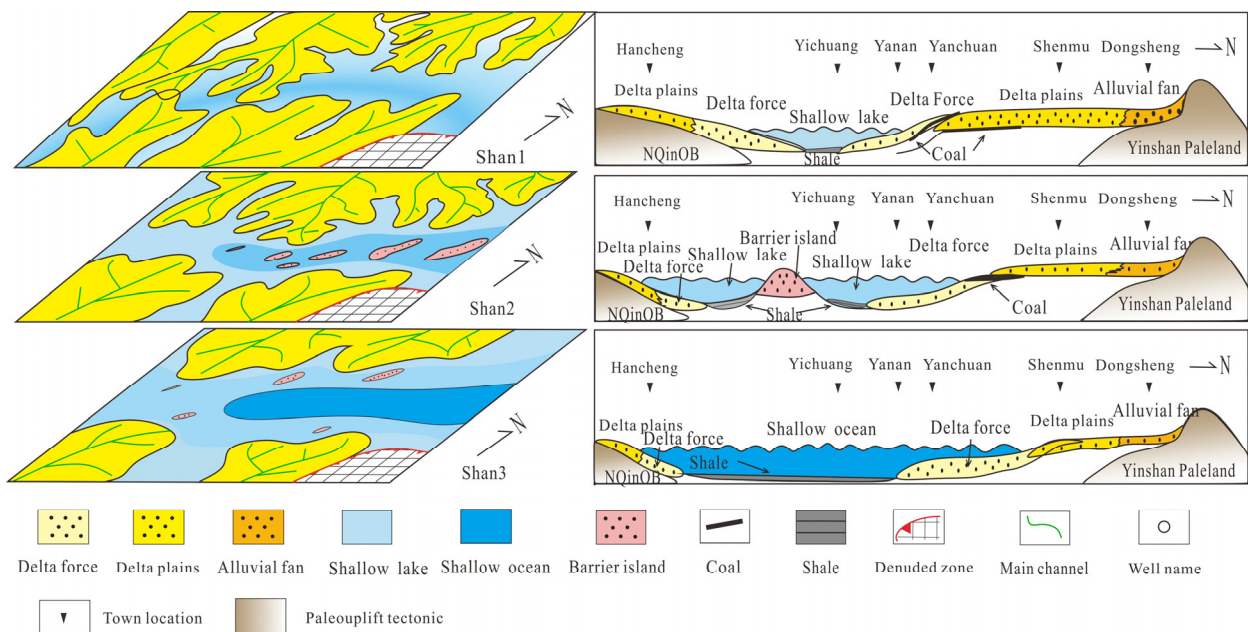


Figure 15. Sedimentary evolution model of the Shanxi Formation in the Ordos Basin.

- (1) Shan3 Section: This stage corresponds to the remnant shallow marine shelf (restricted marginal sea basin). During this phase, the North China Sea and the Qilian Sea encroached from the east and west, respectively, and encountered the central uplift. In response to changes in the stress field to the north and south of the basin, the transverse range expanded continuously until it overlapped with the central uplift. This geological process formed the depositional environment of a remnant shallow marine shelf, characterized by the deposition of organic-rich shale and coal seams;
- (2) Shan2 Section: This stage represents the barrier island–lagoon–coastal environment (remnant land–marginal sea–offshore lake basin). The Ordos Block underwent uplift due to collision with the Central Asian orogenic belt to the north and the Qinling Block to the south. The northern and southern parts of the Ordos Basin featured numerous north–south-oriented braided rivers. The coastline began to retreat from the eastern and western margins of the basin, resulting in diminishing differences between the eastern and western parts of the basin. In contrast, differences between the northern and southern regions of the basin increased. This period was marked by intermittent transgression, and the sedimentation was characterized by sand–mud interbedding;
- (3) Shan1 Section: This stage represents deltaic deposition in an inland depression lake basin. The coastline had completely withdrawn from the basin, initiating a new phase characterized by an inland depression lake basin. In this environment, the Ordos Basin saw the development of a shallow-water braided-river delta depositional system. As tectonic activities waned and slopes reduced, it evolved into a depositional system dominated by a shallow river delta, with the widespread distribution of the riverborne sand bodies.

6. Conclusions

- (1) The detrital zircons found in the study area, dating back to approximately 320–290 Ma, closely match the zircons found in the Carboniferous–Triassic sandstones in the Liouyehe Intermontane Basin. During the Late Paleozoic, the NQinOB not only served as a significant material source in the southeastern Ordos Basin, but it also witnessed a crucial tectono-thermal event. This event occurred after oceanic subduction and continental collision around 320–290 Ma, creating favorable conditions for the maturation of organic matter;

- (2) From the Taiyuan to Shihezi periods, there was a gradual decline in the paleosalinity, as indicated by the decreasing Sr/Ba and B/Ga ratios. The depositional environment of the Shan3 section gradually transitioned into a deltaic setting, building upon the legacy of the land–sea interface from the Taiyuan period. This transition continued until the Shan1 section, when a fully developed shallow-water braided-river deltaic depositional system emerged within the context of inland lakes and basins;
- (3) The sedimentary evolution of the P₁s is divided into three stages: remnants of the shallow-marine-land-shelf, barrier island–lagoon–coastal, and deltaic deposition. The shoreline frequently migrated on the surface, resulting in a wide influence over the water body. Multiple sets of vertically stacked reservoir sandstone bodies alternated with mudstones, shales, and coal seams, forming a well-configured coal system with significant implications for gas storage relationships.

Author Contributions: Conceptualization, W.T. and J.L.; methodology, J.L. and X.L.; software, D.S.; validation, J.L., W.T. and Y.Z.; formal analysis, C.X., Y.Z. and J.X.; investigation, Y.Z.; resources, W.T.; data curation, X.L. and W.T.; writing—original draft preparation, J.L.; writing—review and editing, J.L. and X.L.; visualization, W.T.; supervision, X.L.; project administration, X.L. and W.T.; funding acquisition, X.L. and W.T. All authors have read and agreed to the published version of the manuscript.

Funding: This research was funded by the National Science and Technology Major Project of China (No. 2016ZX05007-003), the Postdoctoral Scientific Research Project of the Shengli Oilfield Company (No. YKB1701), the Science and Technology Project of Petro China (No. T11083), and the Fundamental Research Funds for the Central Universities (Nos. 2020YJSMT02 and 2021YJSMT09).

Data Availability Statement: Not applicable.

Acknowledgments: We are indebted to Jizhen Zhang and Qiang Wei for their insightful, constructive comments on and suggestions for the original manuscript.

Conflicts of Interest: The authors declare no conflict of interest.

References

1. Wang, X.Z. Major breakthrough of gas exploration in Yangchang blocks and its significance. *Oil Gas Geol.* **2014**, *35*, 1–9. (In Chinese)
2. Zhao, Q.P.; Wang, R.G.; Gao, F.; Yin, X. Provenance analysis of Upper Paleozoic in Yanchang Blocks, the Southeast Ordos Basin. *J. Northwest Univ. (Nat. Sci. Ed.)* **2015**, *45*, 933–941. (In Chinese)
3. Zhou, J.S.; Wang, N.X.; Zhao, Q.P.; Yin, X.; Lin, G.F.; Cao, Y.; Li, Y.Y.; Han, X.Q. Natural gas accumulation characteristics in the Upper Paleozoic in the Yanchang exploration block of southeastern Ordos Basin. *Nat. Gas Ind.* **2014**, *34*, 34–41. (In Chinese)
4. Cao, Y.; Yin, X.; Zhao, Q.P.; Wang, G.N. Characteristics and exploration direction of Upper Paleozoic source rock in Yanchang Block of southern Ordos Basin. *China Pet. Explor.* **2015**, *20*, 13–21. (In Chinese)
5. Fu, S.T.; Tian, J.C.; Chen, H.T.; Hou, J.Z.; Zhang, J.Q.; Liu, W.J.; Yang, H.; Fu, J.H.; Fna, Z.P.; Shi, X.Y. The delta depositional system distribution of Late Paleozoic Era in Ordos Basin. *J. Chengdu Univ. Technol. (Sci. Technol. Ed.)* **2003**, *30*, 236–241. (In Chinese)
6. Chen, A.Q.; Chen, H.D.; Xiang, F.; Hou, Z.J.; Lin, L.B.; Xu, S.L. Delta deposits in the Shanxi and Shangshihezi Formations in the northeastern Ordos Basin. *J. Stratigr.* **2010**, *34*, 97–105. (In Chinese)
7. Hao, A.W.; Pu, R.H.; Guo, X.D. Evidences of fluvial deposition of Shanxi Formation in central Ordos Basin. *J. Northwest Univ. (Nat. Sci. Ed.)* **2011**, *41*, 480–484. (In Chinese)
8. Zhu, H.T.; Chen, K.Y.; Liu, K.Y.; He, S. Evidences for deposits of fluvial facies in Shanxi Formation in northeastern Ordos Basin. *Nat. Gas Ind.* **2007**, *27*, 68–70.
9. Zhu, T.; Cui, Z.L.; Yan, Y.K.; Yu, J.; Yu, B.; Guo, X.D.; Liu, B.P. Deposits of sea facies of Shanxi formation in Yan'an district of Ordos Basin. *Geol. Sci. Technol. Inf.* **2011**, *30*, 19–22. (In Chinese)
10. Ye, L.M.; Qi, T.J.; Peng, H.Y. Depositional environment analysis of Shanxi Formation in eastern Ordos Basin. *Acta Sedimentol. Sin.* **2008**, *26*, 202–210.
11. Zhao, J.H.; Jin, Z.J.; Jin, Z.K.; Wen, X.; Gen, Y.K. Lithofacies types and sedimentary environment of shale in Wufeng–Longmaxi Formation, Sichuan Basin. *Acta Pet. Sin.* **2016**, *37*, 572–586. (In Chinese)
12. Kuang, L.C.; Dong, D.Z.; He, W.Y.; Wen, S.M.; Sun, S.S.; Li, S.X.; Qiu, Z.; Liao, X.W.; Li, Y.; Wu, J.; et al. Geological characteristics and development potential of transitional shale gas in the east margin of the Ordos Basin, NW China. *Pet. Explor. Dev.* **2020**, *47*, 435–446. [[CrossRef](#)]

13. Li, Y.; Tang, D.Z.; Wu, P.; Niu, X.L.; Wang, K.; Qiao, P.; Wang, Z.S. Continuous unconventional natural gas accumulations of Carboniferous-Permian coal-bearing strata in the Linxing area, northeastern Ordos Basin, China. *J. Nat. Gas Sci. Eng.* **2016**, *36*, 314–327. [[CrossRef](#)]
14. Li, Y.; Wang, Z.S.; Gan, Q.; Niu, X.L.; Xu, W.K. Paleoenvironmental conditions and organic matter accumulation in Upper Paleozoic organic-rich rocks in the east margin of the Ordos Basin, China. *Fuel* **2019**, *252*, 172–187. [[CrossRef](#)]
15. Li, X.Q.; Wang, Y.; Zhang, J.Z.; Guo, M.; Zhao, P.; Yang, J.; Wang, F.Y. Pore characteristics of shale gas reservoirs from the Lower Paleozoic in the southern Sichuan Basin, China. *J. Nat. Gas Geosci.* **2016**, *1*, 195–202. [[CrossRef](#)]
16. Guo, W.; Liu, H.L.; Xue, H.Q.; Lan, C.L.; Tang, X.Q. Depositional facies of Permian Shanxi Formation gas shale in the northern Ordos Basin and its impact on shale reservoir. *Acta Geol. Sin.* **2015**, *89*, 931–941. [[CrossRef](#)]
17. Du, W.; Jiang, Z.X.; Zhang, Y.; Xu, J. Sequence stratigraphy and sedimentary facies in the lower member of the Permian Shanxi Formation, northeastern Ordos Basin, China. *J. Earth Sci.* **2013**, *24*, 75–88. [[CrossRef](#)]
18. Chen, Y.H.; Wang, Y.B.; Guo, M.Q.; Wu, H.Y.; Li, J.; Wu, W.T.; Zhao, J.Z. Differential enrichment mechanism of organic matters in the marine–continental transitional shale in northeastern Ordos Basin, China: Control of sedimentary environments. *J. Nat. Gas Sci. Eng.* **2020**, *83*, 103625. [[CrossRef](#)]
19. Yao, Y.B.; Liu, D.M.; Tang, D.Z.; Tang, S.H.; Huang, W.H. Practical characterization of adsorption-pores of coals from North China: An investigation on CH₄ adsorption capacity of coals. *Int. J. Coal. Geol.* **2008**, *73*, 27–42. [[CrossRef](#)]
20. Gehrels, G. Detrital zircon U-Pb geochronology applied to tectonics. *Annu. Rev. Earth Planet. Sci.* **2014**, *42*, 127–149. [[CrossRef](#)]
21. Mueller, P.; Langone, A.; Patacci, M.; Giulio, A. Towards a Southern European Tethyan Palaeomargin provenance signature: Sandstone detrital modes and detrital zircon U-Pb age distribution of the Upper Cretaceous-Paleocene Monte Bignone Sandstones (Ligurian Alps, NW Italy). *Int. J. Earth Sci.* **2020**, *109*, 201–220. [[CrossRef](#)]
22. Liu, M.; Zhang, D.; Xiong, G.; Zhao, H.; Di, Y.; Wang, Z.; Zhou, Z. Zircon U-Pb age, Hf isotope and geochemistry of Carboniferous intrusions from the Langshan area, Inner Mongolia: Petrogenesis and tectonic implications. *J. Asian Earth Sci.* **2016**, *120*, 139–158. [[CrossRef](#)]
23. Malusà, M.G.; Villa, I.M.; Vezzoli, G.; Garzanti, E. Detrital geochronology of unroofing magmatic complexes and the slow erosion of Oligocene volcanoes in the Alps. *Earth Planet. Sci. Lett.* **2011**, *301*, 324–336. [[CrossRef](#)]
24. Zhang, J.Z.; Li, X.Q.; Zhang, G.W.; Zou, X.Y.; Wang, F.Y.; Tang, Y.J. Microstructural investigation of different nanopore types in marine continental transitional shales: Examples from the Longtan formation in Southern Sichuan Basin, south China. *Mar. Pet. Geol.* **2019**, *110*, 912–917. [[CrossRef](#)]
25. Tang, X.; Zhang, J.; Wang, X.; Yu, B.; Ding, W.; Xiong, J.; Yang, Y.; Wang, L.; Yang, C. Shale characteristics in the Southeastern Ordos Basin, China: Implications for hydrocarbon accumulation conditions and the potential of continental shales. *Int. J. Coal Geol.* **2014**, *128–129*, 32–46. [[CrossRef](#)]
26. Furmann, A.; Mastalerz, M.; Schimmelmann, A.; Pedersen, P.K.; Bish, D. Relationships between porosity, organic matter, and mineral matter in mature organic-rich marine mudstones of the Belle Fourche and Second White Specks formations in Alberta, Canada. *Mar. Pet. Geol.* **2014**, *54*, 65–81. [[CrossRef](#)]
27. Sun, M.D.; Yu, B.S.; Hu, Q.H.; Chen, S.; Xia, W.; Ye, R.C. Nanoscale pore characteristics of the lower cambrian niutitang formation shale: A case study from well yulce #1 in the southeast of chongqing, China. *Int. J. Coal Geol.* **2016**, *154–155*, 16–29.
28. Zhu, X.; Cai, J.; Wang, X.; Zhang, J.; Xu, J. Effects of organic components on the relationships between specific surface areas and organic matter in mud rocks. *Int. J. Coal Geol.* **2014**, *133*, 24–34. [[CrossRef](#)]
29. Zhang, H.F.; Lu, H.; Zhou, D.W.; Zhang, J.; Dong, Y.P.; Zhang, G.W. The meta-gabbroic complex of Fushui in north Qinling orogen: A case of syn-subduction mafic magmatism. *Gondwana Res.* **2015**, *28*, 262–275. [[CrossRef](#)]
30. Dong, Y.P.; Santosh, M. Tectonic architecture and multiple orogeny of the Qinling Orogenic Belt, Central China. *Gondwana Res.* **2016**, *29*, 1–40. [[CrossRef](#)]
31. Chen, H.D.; Li, J.; Zhang, C.G.; Chen, L.X.; Cheng, L.J. Discussion on the sedimentary environment of the Shanxi Formation in the Ordos Basin and its geological implications. *Acta Petrol. Sin.* **2011**, *27*, 2213–2229. (In Chinese)
32. Wang, X.Z.; Zhou, J.S. Provenance system and sedimentary evolution model of the second member of the Lower Permian Shanxi Formation in the southeast of Ordos Basin. *Nat. Gas Ind.* **2017**, *37*, 9–17. (In Chinese)
33. Zhai, M.G.; Santosh, M. Metallogeny of the North China Craton: Link with secular changes in the evolving Earth. *Gondwana Res.* **2013**, *24*, 275–297. [[CrossRef](#)]
34. Zhou, J.B.; Wilde, S.A. The crustal accretion history and tectonic evolution of the NE China segment of the Central Asian Orogenic Belt. *Gondwana Res.* **2013**, *23*, 1365–1377. [[CrossRef](#)]
35. Yang, Z.; Dong, Y.P.; Zhou, D.W.; Yu, J.; Ma, H.Y. Geochemistry and geological significance of basic rocks in the Xiaomoling complex in the Zhashui area, South Qinling, China. *Geol. Bull. China* **2008**, *27*, 611–617. (In Chinese)
36. Zhao, G.; Cawood, P.A. Precambrian geology of China. *Precambrian Res.* **2012**, *222–223*, 13–54. [[CrossRef](#)]
37. Wang, W.; Zhou, M.F.; Yan, D.P.; Li, J.W. Depositional age, provenance, and tectonic setting of the Neoproterozoic Sibao Group, southeastern Yangtze Block, South China. *Precambrian Res.* **2012**, *192*, 107–124. [[CrossRef](#)]
38. Yuan, H.; Gao, S.; Liu, X.; Li, H.; Günther, D.; Wu, F. Accurate U-Pb age and trace element determinations of zircon by laser ablation-inductively coupled plasma-mass spectrometry. *Geostand. Geoanalytical Res.* **2004**, *28*, 353–370. [[CrossRef](#)]
39. Diwu, C.R.; Sun, Y.; Zhang, H.; Wang, Q.; Guo, A.L.; Fan, L.G. Episodic tectonothermal events of the western North China Craton and NQinOB in central China: Constraints from detrital zircon U-Pb ages. *J. Asian. Earth. Sci.* **2012**, *47*, 107–122. [[CrossRef](#)]

40. Wang, J.Q.; Liu, X.M. Proficiency Testing of the XRF Method for Measuring 10 Major Elements in Different Rock Types. *Rock Miner. Anal.* **2016**, *35*, 145–151. (In Chinese)
41. Belousova, E.; Griffin, W.; O'Reilly, S.Y.; Fisher, N. Igneous zircon: Trace element composition as an indicator of source rock type. *Contrib. Miner. Petrol.* **2002**, *143*, 602–622. [[CrossRef](#)]
42. Jiang, Z.W.; Luo, J.L.; Liu, X.S.; Hu, X.Y.; Ma, S.W.; Hou, Y.D.; Fan, L.Y.; Hu, Y.H. Provenance and Implication of Carboniferous–Permian Detrital Zircons from the Upper Paleozoic, Southern Ordos Basin, China: Evidence from U–Pb Geochronology and Hf Isotopes. *Minerals* **2020**, *256*, 265. [[CrossRef](#)]
43. Nesbitt, H.W.; Young, G.M. Early Proterozoic climates and plate motions inferred from major element chemistry of lutites. *Nature* **1982**, *299*, 715–717. [[CrossRef](#)]
44. Cox, R.; Lowe, D.R.; Cullers, R.L. The influence of sediment recycling and basement composition on evolution of mudrock chemistry in the southwestern United States. *Geochim. Cosmochim. Acta* **1995**, *59*, 2919–2940. [[CrossRef](#)]
45. Roser, B.P.; Korsch, R.J. Provenance signatures of sandstone–mudstone suites determined using discriminant function analysis of major-element data. *Chem. Geol.* **2008**, *67*, 119–139. [[CrossRef](#)]
46. Wang, H.J.; Chen, D.L.; Ren, Y.F.; Zhu, X.H.; Gong, X.K. The relationship between the North Qinling Belt and the North China Craton: Constraints from zircon U–Pb geochronology and metamorphism of metaclastic rocks from the Kuanping Complex. *Acta Petrol. Sin.* **2021**, *37*, 1489–1507.
47. Yang, W.; Yang, J.; Wang, X.; Du, Y. Uplift–denudation history of the Qinling orogen: Constrained from the detrital–zircon U–Pb geochronology. *J. Asian Earth Sci.* **2014**, *89*, 54–65. [[CrossRef](#)]
48. Li, Z.H.; Qu, H.J.; Gong, W.B. Late Mesozoic basin development and tectonic setting of the northern North China Craton. *J. Asian Earth Sci.* **2015**, *114*, 115–139. [[CrossRef](#)]
49. Xie, X.Y. Provenance and sediment dispersal of the Triassic Yanchang Formation, southwest Ordos Basin, China, and its implications. *Sediment. Geol.* **2016**, *335*, 1–16. [[CrossRef](#)]
50. Liu, S.; Su, S.; Zhang, G. Early Mesozoic basin development in North China: Indications of cratonic deformation. *J. Asian Earth Sci.* **2013**, *62*, 221–236. [[CrossRef](#)]
51. Santosh, M.; Yang, Q.Y.; Teng, X.M.; Tang, L. Paleoproterozoic crustal growth in the North China Craton: Evidence from the Liuliang Complex. *Precambrian Res.* **2015**, *263*, 197–231. [[CrossRef](#)]
52. Dong, Y.P.; Zhang, G.W.; Neubauer, F.; Liu, X.M.; Genser, J.; Hauzenberger, C. Tectonic evolution of the Qinling orogen, China: Review and synthesis. *J. Asian Earth Sci.* **2011**, *41*, 213–237. [[CrossRef](#)]
53. Gao, C.Y.; Guo, A.L.; Li, X.H.; Li, K.; Liu, W.G. LA–ICP–MS U–Pb dating of detrital zircon from Liuyehe basin in North Qinling Mountains. *Geol. Bull. China* **2015**, *34*, 1689–1698. (In Chinese)
54. Dong, X.J.; Xu, Z.Y.; Liu, Z.H.; Sha, Q. 2.7 Ga Granitic Gneiss in the Northern Foot of Daqingshan Mountain, Central Inner Mongolia, and Its Geological Implications. *Earth Sci.* **2012**, *31*, 20–27. (In Chinese)
55. Ma, X.D.; Fan, H.H.; Santosh, M.; Ma, J.H. Petrology and geochemistry of the Guyang hornblendite complex in the Yinshan block, North China Craton: Implications for the melting of subduction–modified mantle. *Precambrian Res.* **2016**, *273*, 38–52. [[CrossRef](#)]
56. Liu, L.; Liao, X.Y.; Wang, Y.W.; Wang, C.; Santosh, M.; Yang, M.; Zhang, C.L.; Chen, D.L. Early Paleozoic tectonic evolution of the NQinOB in Central China: Insights on continental deep subduction and multiphase exhumation. *Earth Sci. Rev.* **2016**, *15*, 58–81. [[CrossRef](#)]
57. Li, Y.L.; Yu, X.H.; Shan, X.; Du, Y.H.; Zhou, J.S.; Han, X.Q. Provenance and sedimentary facies of He8 member of Xiashihezi Formation in southeastern Ordos Basin. *J. Northeast Pet. Univ.* **2016**, *40*, 51–60. (In Chinese)
58. Wang, R.; Luo, S.S.; Wang, X.; Lv, Q.Q.; Wang, H.W.; Liu, B.X.; Liu, J. Analysis and identification of provenance of 8th member of Shihezi Formation in the southwestern Ordos Basin. *J. Oil Gas Technol.* **2014**, *36*, 26–29. (In Chinese)
59. Li, H.Y.; He, B.; Xu, Y.G.; Huang, X.L. U–Pb and Hf isotope analyses of detrital zircons from Late Paleozoic sediments: Insights into interactions of the North China Craton with surrounding plates. *J. Asian Earth Sci.* **2010**, *39*, 335–346. [[CrossRef](#)]
60. Qu, H.J.; Ma, Q.; Gao, S.L.; Mei, Z.C.; Miao, J.Y. On Provenance of the Permian in the Southeastern Ordos Basin. *Acta Geol. Sin.* **2011**, *85*, 979–986. (In Chinese)
61. Li, W.J.; Yin, C.Q.; Long, X.P.; Zhang, J.; Xia, X.P.; Wang, L.J. Paleoproterozoic S-type granites from the Helanshan Complex in Inner Mongolia: Constraints on the provenance and the Paleoproterozoic evolution of the Khondalite Belt, North China Craton. *Precambrian Res.* **2017**, *299*, 195–209. [[CrossRef](#)]
62. He, X.L.; Yin, C.Q.; Long, X.P.; Qian, J.H.; Wang, L.J.; Qiao, H.Z. Archean to Paleoproterozoic continental crust growth in the Western Block of North China: Constraints from zircon Hf isotopic and whole-rock Nd isotopic data. *Precambrian Res.* **2017**, *303*, 105–116. [[CrossRef](#)]
63. Dong, Y.P.; Yang, Z.; Liu, X.M.; Zhang, X.N.; He, D.F.; Li, W.; Zhang, F.F.; Sun, S.S.; Zhang, H.F.; Zhang, G.W. Neoproterozoic amalgamation of the Northern Qinling terrain to the North China Craton: Constraints from geochemistry of the Kuanping ophiolite. *Precambrian Res.* **2014**, *255*, 77–95. [[CrossRef](#)]
64. Diwu, C.R.; Sun, Y.; Liu, L.; Zhang, C.L.; Wang, H.L. The disintegration of Kuanping Group in North Qinling orogenic belts and Neo-proterozoic N-MORB. *Acta Petrol. Sin.* **2010**, *26*, 2025–2038. (In Chinese)
65. Guo, Y.H.; Liu, H.J.; Quan, B.; Wang, Z.C.; Qian, K. Late Paleozoic sedimentary system and paleo geographic evolution of Ordos area. *Acta Sedimentol. Sin.* **1998**, *16*, 44–51. (In Chinese)

66. Liu, J.D.; Tian, J.C.; Zhang, X.; Zhang, S.N.; Nie, Y.S.; Zhao, Q.; Wei, D.X. Depositional markers of marine transition facies and its evolution of member 1 of Shanxi Formation, Tabamiao area, North Ordos Basin. *Acta Sedimentol. Sin.* **2006**, *24*, 36–42. (In Chinese)
67. Zhou, Q. Comprehensive Study of High-Resolution Sequence Stratigraphy and Storage Sandbody of the Second Member of Shanxi Formation in Ordos Basin. Ph.D. Thesis, Chengdu University of Technology, Chengdu, China, 2009.
68. Zheng, R.C.; Liu, M.Q. Study on palaeosalinity of Chang-6 oil reservoir set in Ordos Basin. *Oil Gas Geol.* **1999**, *20*, 22–25.
69. Yan, Q.S.; Zhang, G.D.; Xiang, L.S.; Wang, H.Z.; Wu, B.Y.; Dong, R.X.; Wang, Y.Y.; Guo, W.Y. Marine inundation and related sedimentary environment of Funing Group (Lower Paleogene), in Jinhu depression, North Jiangsu Plain. *Acta Geol. Sin.* **1979**, *53*, 74–85. (In Chinese)
70. Sun, Y.; Jiang, Y.Q.; Xiong, X.Y.; Li, X.T.; Li, S.X.; Qiu, Z.; Sun, X.W. Lithofacies and sedimentary environment evolution of the Shan2³ Submember transitional shale of the Shanxi Formation in the Daning-Jixian area, eastern Ordos Basin. *Coal Geol. Explor.* **2022**, *50*, 104–114.

Disclaimer/Publisher's Note: The statements, opinions and data contained in all publications are solely those of the individual author(s) and contributor(s) and not of MDPI and/or the editor(s). MDPI and/or the editor(s) disclaim responsibility for any injury to people or property resulting from any ideas, methods, instructions or products referred to in the content.